MODELS FOR THE GRAVITATIONAL FIELD OF THE GALACTIC BAR. AN APPLICATION TO STELLAR ORBITS IN THE GALACTIC PLANE AND ORBITS OF SOME GLOBULAR CLUSTERS

Bárbara Pichardo [1,2], Marco Martos [1], Edmundo Moreno [1]

ABSTRACT

We built three models for the gravitational field of the Galactic bar. These models are an inhomogeneous ellipsoid, an inhomogeneous prolate spheroid, and a superposition of four inhomogeneous ellipsoids. Among the three models, the superposition provides our best approximation to the observed boxy mass distribution of the Galactic bar. Adding the bar component to an axisymmetric Galactic model, we have calculated stellar midplane orbits and orbits of some globular clusters with known kinematical data. For all models we find a secular dispersion effect upon the orbital energy and angular momentum, as measured in the Galactic inertial frame. This effect might be relevant to explain the orbital prograde-retrograde distribution of globular clusters. For the stellar kinematics, we study the connection between the sense of orbital motion in the midplane and the onset of chaos in the presence of the bar. In the inner region of the bar, chaos is induced by an axisymmetric central component (bulge) and it arises in orbits that change its orbital sense from prograde to retrograde and vice versa as seen from an inertial reference frame. Outside the bar region, chaos appears only in prograde orbits. Our results concerning such connection are consistent and extend those obtained for midplane orbits in the presence of only a spiral pattern in the axisymmetric Galactic model.

Subject headings: galaxies: internal motions —bars— Galaxy: stellar dynamics

[1]Instituto de Astronomía, Universidad Nacional Autónoma de México, A.P. 70-264, 04510 México D.F., México; Electronic mail: barbara@astroscu.unam.mx, marco@astroscu.unam.mx; edmundo@astroscu.unam.mx

[2]Astronomy Department, University of Wisconsin at Madison, 475 N.Charter Street, Madison WI 53706, USA. Electronic mail: barbara@astro.wisc.edu

1. INTRODUCTION

In the past few years it has been finally accepted the existence of a bar in the center of our Galaxy. Some studies providing evidence for this Galactic component are the kinematical data obtained in HI 21-cm emission, CO, and CS (Sanders & Prendergast 1974; Liszt & Burton 1980; Gerhard & Vietri 1986; Binney *et al.* 1991), the Galactic center stellar distribution with Mira Variables from IRAS (Harmon & Gilmore 1988; Nakada *et al.* 1991; Weinberg 1992), and the results of the COBE/DIRBE satellite (Weiland *et al.* 1994, and models based on these observations, such as Dwek *et al.* 1995; Fux 1997; Freudenreich 1998; Beaulieu *et al.* 2000; Bissantz *et al.* 2003). Based on these evidences and due to the expected importance of a non-axisymmetric galactic component to the stellar and gas dynamics, we have constructed three models for the gravitational potential of the Galactic bar and studied their dynamical effects on point masses orbiting the Galaxy.

Several authors have studied and modeled in many ways the gravitational potential of bars. The simplest model is the two-dimensional one, for which the potential has the form $\Phi_{Bar}(R, \varphi) = g(R)cos(2\varphi)$ (Contopoulos & Papayannopoulos 1980); R, φ are polar coordinates in the Galactic plane, φ being measured with respect to the long axis of the bar; g is the amplitude. Other models consider a three-dimensional mass distribution with similar stratification in ellipsoids or prolate spheroids given by

$$\rho_{Bar}(x, y, z) = \begin{cases} \rho_c(1 - m^2)^n, & m \leq 1, \\ 0, & m \geq 1, \end{cases} \tag{1}$$

with ρ_c the central density, $m^2 = \frac{x^2}{a^2} + \frac{y^2}{b^2} + \frac{z^2}{c^2}$, and $a > b \geq c$ the respective semi-axes (ellipsoid: $a > b > c$; prolate spheroid: $a > b = c$).

With n an integer, the density in equation (1) corresponds to Ferrers ellipsoids (Ferrers 1877). The ellipsoidal case with $n = 0$, i.e., an homogeneous ellipsoid, has been considered by Sanders & Tubbs (1980). Inhomogeneous cases ($n \neq 0$) with a prolate shape have been considered by Papayannopoulos & Petrou (1983); Petrou & Papayannopoulos (1983); Athanassoula *et al.* (1983); Teuben & Sanders (1985); Shlosman & Heller (2002). Inhomogeneous ellipsoidal models are considered by Pfenniger (1984), and Kaufmann & Contopoulos (1996).

A more elaborated model has been presented by Zhao (1996), who employed the multipolar expansion technique given by Hernquist & Ostriker (1992) to obtain the gravitational potential of a "boxy" mass distribution that is observed in iso-density contours of edge-on galaxies, and in our own Galaxy as well (Freudenreich 1998).

With the purpose of building a complete three-dimensional model for the Milky Way, we have modeled the Galactic bar in three different ways using the available observational parameters; the main parameter being the observed density (Freudenreich 1998; see Section 3), that cannot be fitted with a simple model such as that of equation (1). Our three models are based on the density considered in Model S of Freudenreich (1998). The first model is an inhomogeneous ellipsoid; the second is an inhomogeneous prolate spheroid, and the third one is a superposition of inhomogeneous ellipsoids. The last model approximates the observed boxy-shaped density stratification of the Galactic bar.

As an application of our models we have analyzed the structure of Poincaré diagrams (or sufrace of section) corresponding to orbits in the Galactic midplane and with the required energy to reach the inner Galactic region. This work extends a recent study in which the structure was explored in a three-dimensional model for the spiral arms (Pichardo *et al.* 2003, hereafter Paper I). In both papers, the axisymmetric background (Galactic) potential is that of Allen & Santillán (1991). A short description of the Galactic model was given in Paper I. The present paper shows also how the kinematics of globular clusters could be altered by the presence of a bar, via numerical integrations of the orbits of six globular clusters in our Galaxy. A more extended and detailed study of the effect of the Galactic bar on the kinematics of the whole sample of globular clusters with known absolute proper motions will be presented in a future paper.

In Section 2 we review the observational parameters of the Galactic bar that are used in our models. In Section 3 we describe the three models for the Galactic bar. Section 4 gives our results: the analysis of stellar midplane orbits (Section 4.1), and the kinematics of six globular clusters (Section 4.2). In Section 5 we discuss the results and give our conclusions. Finally in the Appendix, we give a detailed analytical description of our three models and we include a force field analysis.

2. OBSERVATIONAL PARAMETERS

In this Section we briefly discuss the observational parameters adopted in our models of the Galactic bar.

The length of the bar. This parameter (the length of the bar) depends on another controversial parameter, namely the position angle of the longest axis of the bar with respect to the line of sight. We have taken, mainly, models based on the COBE/DIRBE maps. In particular, for a position angle $\varphi = 20^\circ$, these models place the end of the bar at the galactocentric distance $R_f = 3.1 - 3.5$ kpc (Freudenreich 1998; Binney, Gerhard &

Spergel 1997; Bissantz & Gerhard 2002). Also based in the COBE/DIRBE data and a Galactic model, for a given angular velocity of the bar, the corotation resonance has been derived, giving $R_{cr} \sim 3.4$ kpc (Bissantz, Englmaier, & Gerhard 2003). This resonance gives a constraint to the maximum length of the bar. These results are as well consistent with observations of OH/IR stars (Sevenster 1999) and IRAS variables (Nikolaev & Weinberg 1997).

Axial ratios. Parametric models based on the COBE/DIRBE data suggest axial ratios of approximately 10:3-4:3. Such ratios are in reasonable agreement with non-parametric models of Bissantz & Gerhard (2002). In this work we take the axial ratios obtained in Model S of Freudenreich (1998). These ratios are 10:3.76:2.59.

Density law. Although exponential bars have been frequently used and/or favored by models and observations in other galaxies (Lerner, Sundin & Thomasson 1999; Combes & Elmegreen 1993), in the case of the Galactic bar it appears that toward its center the density profile is not exponential, but a flatter function of the radius (Alard 2001). We have adopted the density law $\rho \propto sech^2(R_S)$, with R_S an effective radius proposed in Model S of Freudenreich (1998) for the Galactic bar. Such model is based on the COBE/DIRBE data set (1.25, 2.2, 3.5, 4.9 μm).

The mass. This is probably the most difficult Galactic parameter to determine, and consequently involves a large uncertainty. Observations with the Space Telescope by Dwek *et al.* (1995) allowed a photometric determination of a mass for the Galactic bulge-bar components of $M_{Bar} \sim 1.3 \times 10^{10}$ M$\odot$. Matsumoto *et al.* (1982) and Kent (1992), using a dynamical bulge modeled as an oblate spheroid, determine theoretically a mass $M_{Bar} \sim 1 \times 10^{10}$ M$\odot$. Zhao (1996), through observations of Galactic microlenses and models restricted by COBE/DIRBE data, finds a best model prediction of $M_{Bar} > 2 \times 10^{10}$ M$\odot$. Weiner & Sellwood (1999) employed a Ferrers bar to perform hydrodynamical simulations which reproduce the *l-v* diagrams in the Galaxy, finding that only a massive bar can produce the huge non-circular motions observed near the Galactic center. In their best model they obtain a value $M_{Bar} \sim 9.8 \times 10^9$ M$\odot$ and also determine the bulge mass, $M_B \sim 5.4 \times 10^9$ M$\odot$.

Angular velocity Ω_{Bar}. The angular speed of the bar is an important dynamical parameter still under debate. Different models and observations report a range of angular speeds; in the last decade, the reported values span the range $40 \leq \Omega_{Bar} \leq 70$ km s^{-1} kpc^{-1}. Usual methods to estimate this parameter are: 1) hydrodynamical simulations, which try to reproduce the *l-v* diagrams of features such as the 3 kpc arm (Englmaier & Gerhard 1999; Fux 1999; Weiner & Sellwood 1999; Bissantz, Englmaier, & Gerhard 2003). 2) The method of "orbital resonances", in which features such as ring-like structures, or observations of

the local velocity distribution, are attributed or related to orbital resonances assuming a Galactic model (for instance, Dehnen 2000). Given the position of the Lindblad inner resonance, v.g., the model predicts an angular speed for the bar. 3) The "direct method" (Tremaine & Weinberg 1984), a kinematic method that does not rely upon a dynamical model. This method utilizes estimations of the surface brightness and measurements of the radial velocity along the nodal line. It has been applied recently to our Galaxy by Debattista, Gerhard & Sevenster (2002) using OH/IR stars. We have adopted, $\Omega_{Bar} = 60$ km s^{-1} kpc^{-1} (Bissantz, Englmaier, & Gerhard 2003). For a review of the observational parameters relevant to the Galactic bar, see Gerhard (2002).

3. GALACTIC BAR MODELS

In this section we make a brief introduction to our three models of the Galactic bar. For a detailed analytical description and an analysis of the force fields, see Sections A, B, C, and D in the Appendix. These models are based on the density Model S of Freudenreich (1998, hereafter MSF), of which some properties have been given in Section 2. The Model S has a density of the form $\rho \propto sech^2(R_S)$, with R_S given by,

$$R_S = \left\{ \left[\left(\frac{|x|}{a_x} \right)^{C_\perp} + \left(\frac{|y|}{a_y} \right)^{C_\perp} \right]^{C_\parallel/C_\perp} + \left(\frac{|z|}{a_z} \right)^{C_\parallel} \right\}^{1/C_\parallel}. \tag{2}$$

With a Sun's galactocentric distance of 8.5 kpc, the scale lengths in the directions x, y, z (the major, middle, and minor semi-axes of the bar lie along these directions respectively) are $a_x = 1.7$ kpc, $a_y = 0.64$ kpc, $a_z = 0.44$ kpc, and the exponents are $C_\parallel = 3.5$, $C_\perp = 1.57$. The effective boundary of the bar on the x-axis has a major semi-axis $a_{Bar} = 3.13$ kpc, which sets the scaled distance $R_{end_S} = a_{Bar}/a_x = 1.841$. In $R_S \geq R_{end_S}$ the density has an additional Gaussian factor with a scale length $h_{end} = 0.46$ kpc; this leads to a steep but smooth fall in density in the outer region.

Our first model for the Galactic bar is triaxial, as it seems to be the general case of galactic bars; it is constructed with an ellipsoid with a *similar* mass distribution (Schmidt 1956) in order to obtain the observed density law in the Galaxy: $\rho \propto sech^2(R_S)$. In the same manner we have constructed a second model with prolate shape that corresponds approximately to the Galactic bar case (Section 2), with the same density stratification as the ellipsoidal one. In both models we take $C_\parallel = C_\perp = 2$ in equation (2), and equal scale lengths in the y and z directions in the prolate case. Our third model, constructed to approximate the boxy mass distribution of MSF, is a superposition of four ellipsoids with

the same density law as the ellipsoidal and prolate models.

The gravitational potential of the modeled Galactic bar is easily obtained from known results in potential theory (see, e.g. Mc Millan 1930; Kellogg 1953).

4. RESULTS

4.1. Orbital Analysis on the Galactic Plane

As a first application of the models given in Section 3, we make an analysis of orbital motion in the Galactic plane. The orbital analysis is made in the non-inertial reference frame attached to the bar, labeled as the primed system of Cartesian coordinates (x', y', z'). The x'-axis is taken as the line along the major axis of the bar, the z'-axis is perpendicular to the Galactic plane, with its positive sense toward the north Galactic pole, and the y'-axis is such that the (x', y', z') axes form a right-handed system. The angular velocity of the Galactic bar, Ω_{Bar}, points in the negative direction of the z'-axis, i.e., a clockwise rotation as seen from the north Galactic pole. We take the mass of the bar as $M_{Bar} = 9.8 \times 10^9$ M$\odot$, and its angular velocity $\Omega_{Bar} = 60$ km s^{-1} kpc^{-1}. The bar is superimposed on a modified version of the axisymmetric Galactic potential of Allen & Santillán (1991).

For motion in the Galactic plane, Jacobi's constant in the non-inertial frame is

$$E_J = \frac{1}{2}(v_x'^2 + v_y'^2) + \Phi_{AS}(x', y') + \Phi_{Bar}(x', y') - \frac{1}{2}\Omega_{Bar}^2(x'^2 + y'^2), \qquad (3)$$

with Φ_{AS} the axisymmetric Galactic potential of Allen & Santillán (1991), and Φ_{Bar} the potential due to the bar. All the computations presented here were done using the Bulirsch-Stoer algorithm of Press *et al.* (1992), conserving Jacobi's constant within a relative variation of $|(E_{Ji} - E_{Jf})/E_{Ji}| \approx 10^{-11}$.

In Paper I we made an analysis of orbital motion in the Galactic plane using a three-dimensional model for the spiral arms. As in that case, a convenient technique in our analysis is the use of Poincaré diagrams, or surfaces of section, and periodic orbits. In Paper I we introduced the concept of *zero angular-momentum separatrix*, loosely defined (but with a physical meaning discussed therein) as the very narrow region in the surfaces of section that cleanly separates prograde and retrograde orbits, as seen from an inertial reference frame. In that work we stress the point that such clean separation will not appear in the customary surface of section diagrams which do not take into account the information from the inertial frame. The reason obeys to the fact that in the usual rotating frame, the

definition of prograde/retrograde is ambiguous, as an orbit may change its sense of motion with time. The separatrix is an exceptional set of orbits: it consists of orbits with nearly zero angular momentum, for which the sign of the angular momentum alternates between positive and negative *in the inertial frame.* The relevance of the distinction between prograde and retrograde orbits is its apparent connection with stochastic motion. For the spiral perturbation, we found chaos only in prograde orbits, a region in the surface of section diagram bounded by the separatrix. In our application of this concept to the Galactic spiral arms, we noticed that when the mass of the arms was larger than a given value, the separatrix became wider. In this section we analyze the behavior of this separatrix under the gravitational potential of the Galactic bar.

Based on observational results, we have considered two experiments with differences in the axisymmetric potential (specifically in the central component). Experiment I takes the axisymmetric potential (halo, disk and bulge) with a bulge of approximately 45% of the mass of the bar. Several authors consider that both structures, bulge and bar, coexist (Norman, Sellwood & Hasan 1996; Sevenster 1999; Weiner & Sellwood 1999; Zhao 2000). In the experiment II the central component (bulge) is completely removed, leaving only the halo and disk of the axisymmetric model, and the bar component. With the purpose of understanding the global effect of the axisymmetric potential, we have added one last experiment where we make the analysis for the bar alone, removing the axisymmetric component (this will be called experiment III).

Figure 1 shows nine Poincaré diagrams for orbits in the presence of the ellipsoidal model of the Galactic bar. Units of Jacobi's constant (E_J in the diagrams) are 100 km^2 s^{-2}. The three diagrams on the top correspond to experiment I, those in the middle to experiment II, and the bottom panels give the results of experiment III. In Figure 2 we present the same experiments as in Figure 1, but now using the prolate model. Figure 3 shows the corresponding results with the model of superposition of ellipsoids.

Comparing families of same E_J for the three different models (ellipsoidal, prolate and the superposition), we find very similar results mainly between ellipsoidal and prolate bars in the 2-D orbital dynamics case (for example the extension of the separatrix, retrograde and prograde regions and the resonant families). Slight differences are found with the superposition model.

Unlike our model with spiral arms (Paper I), where the separatrix was defined by a very narrow curve in phase space, we notice that in all our models with the bar potential, the separatrix (which is shown in all the phase space diagrams -Figures 1, 2, 3, 4, 5, 6- in darker points) is considerably wider; i.e., we have more orbits that change their sense of motion from prograde to retrograde, and vice versa, *as seen from an inertial reference*

frame. The width of this region depends on the relative importance between the mass of the bar and the mass of the central component (like a bulge). Orbits in this region might result interesting, since orbital chaos seems to present a trend to appear first in this type of orbits.

With the model of the ellipsoidal bar, in those cases that include a central component, or bulge (experiment I), for low values of E_J (=-2800, for example) the inner and most tied orbits are completely ordered. For other values of E_J (=-2300, for example), the onset of chaos occurs in orbits belonging to the separatrix. Beyond the corotation barrier (approximately located at 3.5 kpc from the Galactic center), chaos dominates the prograde orbital region. As in the case of the spiral perturbation (Paper I), there is no chaos in the retrograde region (as seen from an inertial reference frame).

To illustrate the behavior in real space of the orbits that compose some Poincaré diagrams, we show in Figures 4, 5, and 6, some examples of orbits in the inertial (upper diagrams), and non-inertial (lower diagrams) frames, with the ellipsoidal bar for experiments I, II, and III. In these diagrams there are some examples of orbits like those that form the prograde region (upper left panels in all cases). These orbits have always a defined sense of motion in the same direction as the bar. On other hand, in the non-inertial frame (bottom panel), orbits have the characteristic changes of orbital sense and self-crossing produced by accelerated reference frames. We also show some examples of the periodic orbits x_1 (lower left panels) and x_4 (lower middle panel in Figure 4). Orbits from the separatrix are also shown (upper panels); these orbits are the ones with the lowest angular momentum of each family E_J.

In the three models, the separatrix widens out going from experiment I to III. This is due to the local effect of the bar on the orbits; i.e., stars feel locally stronger forces, due to the bar, than the axisymmetric force field that tends to force them to travel in orbits with no change in the sense of rotation, as seen from an inertial reference frame. On these grounds, we expect that, in galaxies where the bulge (or any central axisymmetric component) is very important relative to the bar (as in early type galaxies), orbits with a non changing sense of motion in the inertial system will dominate. On the other hand, in galaxies where the central component is less important relative to the non-axisymmetric component, orbits with a changing sense of motion from prograde to retrograde and vice versa in the inertial frame would be more important.

Regarding to chaos, Athanassoula (1990) finds that boxy-shape bars produce more chaos in the orbital dynamics than elliptical bars, however this model is two dimensional. This particular result is not reproduced in our case, with a three dimensional bar potential, where we find that chaotic regions in phase space are very similar in its extension, and even

in shape, to the results with the ellipsoidal and prolate bars.

On the other hand, we notice, comparing experiments I, II and III (for any of our three bar models), that when the bulge is removed, chaos disappears in orbits in the inner regions – inside the extent of the bar –. That is, the bar seems to be favored if there is no central spherical component. The more massive is the bulge component, the wider is the chaotic region in the inner region of the bar, until this region covers all phase space, growing rapidly and destroying the x_1 periodic orbits (this result is also obtained by Hasan & Norman 1990, in a prolate spheroid, but the central component is in this case a black hole). When the central spheric component is dominant, the bar tends to disappear; in this case planar orbits would be fully ordered again. Teuben & Sanders (1985) find the same results in this direction.

Chaos appears for some orbital families (the less tied up), and for the parameters we have taken for the Galactic bar, it appears only in the orbits that form the separatrix for the inner region of the bar, and only in the prograde orbits for the outer regions of the bar, crossing the corotation barrier. This last result (also found by Fux 2001, and Pfenniger 1984) is reproduced in all our models, unlike Athanassoula et $al.$ (1983) who find that chaos is not present in orbits that reach corotation. Retrograde orbits do not present chaos in any case (detailed results in these direction will be presented in a future paper).

The shape of the so called x_1 periodic orbits seems to be related with the real shape of bars (Teuben & Sanders 1985). We have constructed some families of these kind of orbits for our ellipsoidal bar. The shape of these sets of orbits is also affected by the presence of central spherical components (like a bulge). In this manner, going from experiments I (top panel of Figure 7) to III (bottom panel of the same Figure), orbits change its shapes going from elliptical to "boxy" figures. The higher the mass of the bulge or any central spherical component is, the rounder the periodic orbits are.

4.2.   Orbits of Some Globular Clusters

Galactic orbits of globular clusters computed in an axisymmetric Galactic potential have been studied by many authors (e.g., Allen & Martos 1988; Allen 1990; Brosche et $al.$ 1991; Dauphole et $al.$ 1996; Dinescu, Girard, & van Altena (1999, DGA99 hereafter); Brosche, Odenkirchen, & Geffert 1999). Properties of the computed orbits (e.g., eccentricity, peri- and apogalactic distances, maximum distance from the Galactic plane, energy, z-component of the angular momentum) have been usually related with the metallicity of the cluster, inferring from this how the Galactic halo and disk were formed. However, the effect

of both the spiral arms and the Galactic bar remains obscure. In this section we compute the orbits of six globular clusters in a Galactic potential which includes the Galactic bar. We use the models for the gravitational potential of the bar presented in Section 3 (better described in the Appendix), superimposed on an axisymmetric mass distribution obtained from the axisymmetric Galactic model of Allen & Santillán (1991). In a more detailed study underway, we analyze the Galactic orbits of the 38 globular clusters with known revised absolute proper motions compiled by DGA99, considering the Galactic bar and the spiral arms.

As in Section 4.1, we take the mass of the bar and its angular velocity as $M_{Bar} = 9.8 \times 10^9$ M$\odot$, $\Omega_{Bar} = 60$ km s^{-1} kpc^{-1}. The mass of the bulge in the Galactic model of Allen & Santillán (1991), $M_B = 1.4 \times 10^{10}$ M$\odot$, is reduced to $M_B = 4.26 \times 10^9$ M$\odot$ to account for the added bar component (thus assuming this bar is part of the bulge).

At time $t = 0$ the major axis of the bar makes an angle of $\sim 20°$ with the Sun-Galactic center line (Freudenreich 1998). We integrate the orbits backward in time during $\sim 1.5 \times 10^{10}$ yr, using the Bulirsch-Stoer algorithm of Press et $al.$ (1992). The orbits are computed in the non-inertial reference frame of the bar (see Section 4.1), where Jacobi's constant can be used to check the numerical integration. In each orbit we localize all the points where the distance to the Galactic center, r, has a local maximum or minimum, and the points where the absolute value of the z- coordinate (perpendicular to the Galactic plane), $|z|$, has a local maximum. An eccentricity $e = (r_{max} - r_{min})/(r_{max} + r_{min})$ is computed with successive values of extrema in r. Also, we compute in the Galactic inertial frame the values of the energy per unit mass, E, and the z- component of the angular momentum per unit mass, h, at all orbital points with an extremum in r or $|z|$. Thus, with E, h at these points we sample the variation of these important quantities, which are otherwise constant when using an axisymmetric Galactic model.

From the 38 globular clusters listed by DGA99, the six clusters we have chosen are among the clusters that according to their Table 5 have perigalactic distances lying in the region of the Galactic bar, as computed in their axisymmetric Galactic model. Thus, we consider a sample of clusters for which the effect of the Galactic bar is expected to be important. The six globular clusters are: NGC 5139 (ω Cen), NGC 6093 (M 80), NGC 6144, NGC 6171 (M 107), NGC 6218 (M 12), and NGC 6712. Table 2 of DGA99 lists the data from which the initial conditions of the orbits can be obtained. The adopted solar motion is $(U, V, W) = $ (-11.0, 14.0, -7.5) km s^{-1} (U positive outward from the Galactic center), 220 km s^{-1} the rotation velocity of the LSR, and 8.5 kpc the Galactocentric distance of the Sun. We have taken into account a misprint in the radial velocity of NGC 6218 listed in Table 2 of DGA99; this velocity is negative, according to Pryor & Meylan (1993). Also, a

minus sign is missing in the U- velocity with respect to the LSR listed for NGC 6144.

In Table 1 we give the orbital properties of the six globular clusters, computed in the axisymmetric Galactic model of Allen & Santillán (1991) during an interval of 1.5×10^{10} yr backward in time. Average values are given for r_{min}, r_{max}, $|z|_{max}$, e, and in the last two columns the values of the constants E, h. Comparable results are listed in Table 5 of DGA99, obtained with their axisymmetric Galactic model.

The orbital properties of the six clusters obtained with the three models of the Galactic bar are presented in Table 2. Minimum and maximum values of E and h are given in the last four columns. The three lines in each entry correspond to the ellipsoidal, prolate, and superposition models, in this order. The average values in this table are computed over the 1.5×10^{10} yr time interval. Negative values of h mean the orbital motion is retrograde, i.e., in the opposite sense to the actual rotation of the bar (or in the same sense of the backward-in-time rotation of the bar). The averages in Table 2 are approximately similar in the three models of the Galactic bar, except in the case of NGC 6093, in which the superposition model gives an orbital evolution quite different from that obtained with the ellipsoidal and prolate models. To illustrate the dependence of the detailed orbital evolution on the model, Figure 8 shows the meridional orbits of NGC 5139, NGC 6093, and NGC 6218. The upper panels give the orbits in the axisymmetric Galactic model of Allen & Santillán (1991), the panels in the second row correspond to the ellipsoidal model, those in the third row correspond to the prolate model, and the panels at the bottom give the orbits in the superposition model. Notice the different scales used in the figure; these scales are the same in a given cluster (except for the orbit of NGC 6218, where the scales are not the same in the vertical and horizontal axes). Comparing with the orbital evolution obtained with the axisymmetric model, this figure shows that the inclusion of the bar can increase the apogalactic distance and the z- distance from the Galactic plane, and also decrease in some times the perigalactic distance. Cases like NGC 6093 computed in the superposition model deserve a more detailed analysis.

In Figure 9 we give the details of the variations of E and h in the orbits of the clusters in Figure 8. In each panel, E is read on the left scale and h on the right scale. The upper, middle, and bottom panels correspond to the ellipsoidal, prolate, and superposition models of the bar, respectively. Figure 9 shows an interesting additional effect which can be produced with the bar: large variations in E and h with the possibility of a change in the sense of orbital rotation, as measured in the Galactic inertial frame. This effect appears in the orbit of NGC 6093 computed with the ellipsoidal and prolate models of the bar; it barely appears at some time with the superposition model (see value of h_{max} in Table 2). We are analyzing this effect particularly in the clusters reaching the inner Galactic region.

This effect might account for the observed retrograde motions in some clusters.

5. CONCLUSIONS

We present three models for the gravitational potential of the Galactic bar, based on the mass distribution for this component given by Model S of Freudenreich (1998). These models are an ellipsoid, a prolate spheroid, and a superposition of four ellipsoids. The models can be easily implemented for a numerical integration of orbits in a non-axisymmetric Galactic potential. In particular, our third model, which is a superposition of four inhomogeneous ellipsoids, gives a good approximation to the boxy mass distribution of the Galactic bar. Thus, in this model the resulting gravitational potential might give relevant results in the analysis of orbits reaching the region of the bar. For orbits lying outside the bar, the detailed modeling of the shape of the bar is less important, and any of the three models can be used.

We have applied our models to orbits in the Galactic plane in the inner Galactic region, and to orbits of some globular clusters. We find that the bar produces a dispersion on the energy and angular momentum, as measured in the Galactic inertial frame. In particular, for orbits with the z- component of angular momentum close to zero, this dispersion effect can make an orbit oscillate between prograde and retrograde, resulting in a wider separatrix. In the case of globular clusters, the bar might be responsible for the observed orbital prograde-retrograde distribution. In general, the relative importance of the bar with respect to a central axisymmetric component determines the dominant stellar sense of motion, i.e., the larger is this ratio (M_{Bar}/M_{Cen}, where M_{Bar} is the bar mass and M_{Cen} is the mass of a central component like a bulge), the larger is the population of stars that will change their sense of motion from prograde to retrograde (and vice versa), as seen from an inertial reference frame.

In a preliminary analysis of chaotic regions, we have found that a central axisymmetric component induces the onset of orbital chaos in the inner region of the bar, and chaos mainly appears in the orbits that change their sense of motion in the inertial frame of reference, i.e. those that form the separatrix. Outside the bar, chaos only appears after the corotation barrier and only in the prograde orbits. As the central component mass is reduced or disappeared, chaos diminishes or is completely removed for orbits in the inner region of the bar. It is remarkable that the connection between stochastic motion and sense of motion measured from the inertial frame, found for the relatively weak spiral perturbation, is preserved under the much stronger perturbation of the bar. However, the properties of the separatrix are still a subject we consider deserves a more detailed study.

For globular clusters, chaos is found (v.g., Allen and Martos 1988) in the axisymmetrical potential with no need of a perturbation such as the presence of a spiral pattern or a bar. Chaos in those systems is seemingly related to the impulsive nature of the rapid passing of the cluster through the large mass concentration at the central regions of the Galaxy. For midplane motion, results concerning the connection between the angular momentum and chaos are apparently indicating that the physical agent has to do with a secular effect; i.e., prograde orbits with respect to the general motion of the perturbing mass, spiral or bar, tell us about longer times under their influence than that from a rapid encounter, as that expected from retrograde motion. A picture able to include a general explanation for both mechanisms triggering chaotic motion with a physical flavor seems necessary. In the case of planar orbits, Paper I invoked the overlapping of resonances as the standard explanation for the different phenomenology between prograde and retrograde motion in regard to stochasticity. In three dimensional motion, resonances involving vertical oscillations could be the lacking piece for a unified scheme.

Acknowledgments

APPENDIX

In this appendix we present the detailed analytic derivation of the potential models for the Galactic bar proposed in this work (briefly described in Section 3).

A. The Ellipsoidal Model

Our first model for the Galactic bar is an inhomogeneous ellipsoid. Its similar mass distribution has a density,

$$
\begin{aligned}
\rho(R_S) &= \rho_0 sech^2(R_S), \quad R_S \leq R_{end_S} \\
\rho(R_S) &= \rho_0 sech^2(R_S)e^{-(R_S-R_{end_S})^2/h_{end_S}^2}, \quad R_S \geq R_{end_S}
\end{aligned}
\tag{A1}
$$

with $R_S = \left\{ \frac{x^2}{a_x^2} + \frac{y^2}{a_y^2} + \frac{z^2}{a_z^2} \right\}^{1/2}$, $h_{end_S} = h_{end}/a_x$. The second line in equation (A1) shows the Gaussian factor. Equation (A1) corresponds to equations (13) and (14) of Freudenreich (1998), but we have corrected a misprint in his Gaussian factor, adapting this as given above.

As in the case of the construction of an inhomogeneous spheroid with *similar* strata using homogeneous spheroidal components (Schmidt 1956), our ellipsoidal model for the bar approximates the density in equation (A1) with a step-stair function. Figure 10 shows the density function normalized by the central density, ρ/ρ_0, vs. R_S. Each stair step represents an homogeneous ellipsoidal component. By taking a large number of these components the accuracy of the approximation improves rapidly.

Since the density function does not have a constant gradient, we have taken three intervals or regions in the scaled distance R_S to specify different number of components according to the dominant gradient of the density function (see Fig. 10). In the inner region the density interval is divided in N_1 subintervals, giving $N_1 - 1$ homogeneous ellipsoidal components, each one with a density $\Delta\rho_1$. The middle and outer regions have, respectively, N_2, N_3 subintervals and components, with corresponding densities $\Delta\rho_2, \Delta\rho_3$. The inner region ends at a major semi-axis a_L, $0 < a_L < a_{Bar}$, i.e., at $R_S = a_{L_S} = a_L/a_x$; the middle region ends at the effective major semi-axis of the bar $R_{end} \equiv a_{Bar} = 3.13$ kpc, i.e., at $R_S = a_{Bar}/a_x \equiv a_{Bar_S} = 1.841$. The outer region contains the Gaussian factor in its density. Figure 10 shows an example with $N_1 = 12$, $N_2 = 15$, $N_3 = 5$, and $a_L = 1.0$ kpc.

This procedure of taking three regions to account for different gradients in density will not have relevance in the limit of large partition numbers (N_1, N_2, N_3), which is ultimately

the limit to consider in this formulism. This analysis will be necessary in our three models; in Section D we give a comparison of the total force fields of the bar obtained with different partitions.

The densities of the ellipsoidal components in the three regions are

$$
\begin{aligned}
\Delta\rho_1 &= \frac{\rho_0}{N_1}\left\{1 - sech^2(a_{L_S})\right\} \\
\Delta\rho_2 &= \frac{\rho_0}{N_2}\left\{sech^2(a_{L_S}) - sech^2(a_{Bar_S})\right\} \\
\Delta\rho_3 &= \frac{\rho_0}{N_3}sech^2(a_{Bar_S}),
\end{aligned}
\tag{A2}
$$

then, with equation (A1) the scaled dimensions R_S of these components in the inner and middle regions are

$$
R_{s_i} = sech^{-1}\left\{1 - \frac{i}{N_1}\left[1 - sech^2(a_{L_S})\right]\right\}^{1/2}, \quad i = 1, 2, ..., N_1 - 1
\tag{A3}
$$

$$
R_{s_{N_1+j}} = sech^{-1}\left\{sech^2(a_{L_S}) - \frac{j}{N_2}\left[sech^2(a_{L_S}) - sech^2(a_{Bar_S})\right]\right\}^{1/2}, \quad j = 0, 1, 2, ..., N_2 - 1
\tag{A4}
$$

In the outer region the scaled dimensions are obtained solving the equation

$$
\left(1 - \frac{k}{N_3}\right)sech^2(a_{Bar_S}) - sech^2 R_{s_{N_1+N_2+k}}e^{-\left(R_{s_{N_1+N_2+k}} - a_{Bar_S}\right)^2/h^2_{end_S}} = 0, \quad k = 0, 1, ..., N_3 - 1
\tag{A5}
$$

Defining $\zeta \equiv a_y/a_x$ and $\xi \equiv a_z/a_x$, the volume of an ellipsoidal component with a scaled major semi-axis $a_{s_l} = R_{s_l}, l = 1, 2, ..., N_1 + N_2 + N_3 - 1$, is $V_l = \frac{4}{3}\pi\zeta\xi a_l^3$, with $a_l = a_{s_l}a_x$. Thus, with $\Delta_1 = \Delta\rho_1/\rho_0$, $\Delta_2 = \Delta\rho_2/\rho_0$, and $\Delta_3 = \Delta\rho_3/\rho_0$ (these quantities obtained in terms of N_1, N_2, N_3 from equation (A2)) the total mass of the ellipsoidal components (= mass of the bar) is

$$
M_{Bar} = \frac{4}{3}\pi\zeta\xi\rho_0\left\{\Delta_1\sum_{i=1}^{N_1-1}a_i^3 + \Delta_2\sum_{j=0}^{N_2-1}a_{N_1+j}^3 + \Delta_3\sum_{k=0}^{N_3-1}a_{N_1+N_2+k}^3\right\}.
\tag{A6}
$$

For a given total mass M_{Bar}, this last equation gives the corresponding central density ρ_0; thus the densities of the components follow from equation (A2). Finally, with the densities and dimensions of these components, their gravitational potentials are obtained with standard potential theory (e.g., Kellogg 1953). The potential of the bar at a given point in space is the sum of these potentials at this point.

B. The Prolate Model

Even though it is believed that bars in general are triaxial structures, there are strong pieces of evidence pointing to an approximately prolate Galactic bar (Freudenreich 1998). Therefore it is appropriate to consider a prolate shape. A model of this type for the Galactic bar is analytically simpler than the ellipsoidal one, and it makes an orbital integration considerably faster.

The density in this model has again the form given in equation (A1), but now $R_S = \left\{ \frac{x^2}{a_{x_p}^2} + \frac{y^2+z^2}{a_{y_p}^2} \right\}^{1/2}$, with $a_{x_p} = a_x$, $a_{y_p} = \frac{1}{2}(a_y + a_z)$.

Schmidt (1956) gives the procedure to obtain the gravitational potential and force due to an oblate spheroid with a *similar* mass distribution $\rho(a)$, where a is the major semi-axis of a *similar* oblate surface. Following his procedure one can readily obtain the corresponding expressions for a prolate spheroid with the same type of mass distribution. With the x-axis being the long axis of the prolate spheroid, at a given point $\mathbf{r} = (x, y, z)$ the acceleration components along and perpendicular to this axis are (in units in which the Universal gravitational constant G = 1)

$$-\frac{\partial \Phi}{\partial x} = -4\pi \ e_p^{-3} \ (1 - e_p^2) \ x \ \int_0^{\beta_p'} \rho(a(\beta_p)) \frac{sin^2\beta_p}{cos\beta_p} d\beta_p, \tag{B1}$$

$$-\frac{\partial \Phi}{\partial R} = -4\pi \ e_p^{-3} \ (1 - e_p^2) \ R \ \int_0^{\beta_p'} \rho(a(\beta_p)) \frac{sin^2\beta_p}{cos^3\beta_p} d\beta_p, \tag{B2}$$

with $e_p = (1 - (\frac{b_{sph}}{a_{sph}})^2)^{1/2}$ the eccentricity of the spheroid, a_{sph}, b_{sph} its major and minor semi-axes, $R = (y^2 + z^2)^{1/2}$, $\beta_p' = sin^{-1} e_p$ if $\mathbf{r}$ is internal to the spheroid, and β_p' the solution of $x^2 sin^2\beta_p' + R^2 \tan^2 \beta_p' = a_{sph}^2 e_p^2$ if $\mathbf{r}$ is an external point. The function $a(\beta_p)$ is obtained from $x^2 sin^2\beta_p + R^2 \tan^2 \beta_p = a^2 e_p^2$.

The potential at an internal point $\mathbf{r}$ is

$$\Phi = -4\pi e_p^{-1}(1 - e_p^2)\left\{\int_0^{a(\mathbf{r})} \rho(a)a\ln\frac{1 + sin\ \beta_p}{cos\beta_p}da + \frac{1}{2}\ln\frac{1 + e_p}{1 - e_p}\int_{a(\mathbf{r})}^{a_{sph}} \rho(a)a\ da\right\}, \quad \text{(B3)}$$

with $a(\mathbf{r}) = \left(x^2 + \frac{R^2}{1-e_p^2}\right)^{1/2}$ the major semi-axis of the *similar* spheroidal surface passing through the point $\mathbf{r}$. If $\mathbf{r}$ is an external point the potential is

$$\Phi = -4\pi\ e_p^{-1}\ (1 - e_p^2)\int_0^{a_{sph}} \rho(a)a\ln\frac{1 + sin\ \beta_p}{cos\beta_p}da. \quad \text{(B4)}$$

Analytical solutions of equations (B1) - (B4) are difficult to obtain for the density of the form of equation (A1) applied to a prolate bar (notice that equation (A1) gives the density at the scaled distance R_S; in equations above we need the density at the *unscaled* semi-axis variable $a = R_S a_{x_p} \equiv R_S a_x$ along the major axis). Thus, we need again an approximation for the density function. Due to the fact that prolate spheroids are mathematically simpler than ellipsoids, we can make a step further in the representation of the density. Instead of a step-stair representation, as in the ellipsoidal model, a better approximation is a set of linear functions, a polygon. With this approximation, the analytical solution of equations (B1) - (B4) is readily obtained for each linear part.

We use the same procedure of assigning a partition in scaled distance R_S as in the ellipsoidal model. First, we re-number the scaled distances $R_{s_l}, l = 1, 2, ..., N_1 + N_2 + N_3 - 1$, taking $n = l + 1$ and $R_{s_1} = 0$. The densities at these re-numbered scaled distances R_{s_n} are $\rho(R_{s_n}), n = 1, 2, ..., N_1 + N_2 + N_3$. Then, with

$$p_{0_n} = \frac{R_{s_{n+1}}\rho(R_{s_n}) - R_{s_n}\rho(R_{s_{n+1}})}{R_{s_{n+1}} - R_{s_n}}, \quad \text{(B5)}$$

$$p_{1_n} = \frac{\rho(R_{s_{n+1}}) - \rho(R_{s_n})}{R_{s_{n+1}} - R_{s_n}}, \quad \text{(B6)}$$

the set of linear functions which approximate the density is

$$\rho_n^\star[R_S] = p_{0_n} + p_{1_n}R_S, \quad R_{s_n} \le R_S \le R_{s_{n+1}}, \quad n = 1, 2, ..., N_1 + N_2 + N_3 - 1. \quad \text{(B7)}$$

In this prolate model we take a linear fall to zero in density at the boundary of the spheroid; then we add an outer partition distance $R_{s_{N_1+N_2+N_3+1}}$

where $\rho^\star_{N_1+N_2+N_3}[R_{s_{N_1+N_2+N_3+1}}] = 0$, and the slope of the linear density $\rho^\star_{N_1+N_2+N_3}[R_S]$, $R_{s_{N_1+N_2+N_3}} \leq R_S \leq R_{s_{N_1+N_2+N_3+1}}$, being the same of $\rho^\star$ in the previous interval in R_S.

For each linear function $\rho^\star_n[R_S]$, the corresponding density function $\rho^\star_n(a)$ giving the density at the *unscaled* variable $a = R_S a_{x_p} \equiv R_S a_x$, is $\rho^\star_n(a) = \rho^\star_n[R_S] = p_{0_n} + p_{1_n} R_S = p_{0_n} + p_{1_n} a/a_x$. The values of a at the scaled partition distances R_{s_n} are $a_n = R_{s_n} a_x$.

The mass of the prolate spheroid (= mass of the bar) under the $\rho^\star$ representation is

$$
\begin{aligned}
M_{Bar} &= 4\pi\,(1 - e_p^2) \sum_{n=1}^{N_1+N_2+N_3} \int_{a_n}^{a_{n+1}} \rho^\star_n(a) a^2 \, da \\
&= 4\pi\,(1 - e_p^2) \sum_{n=1}^{N_1+N_2+N_3} \left[\frac{1}{3} p_{0_n} \left(a_{n+1}^3 - a_n^3 \right) + \frac{1}{4} \frac{p_{1_n}}{a_x} \left(a_{n+1}^4 - a_n^4 \right) \right].
\end{aligned}
\tag{B8}
$$

The coefficients p_{0_n} and p_{1_n} are obtained with equations (B5) and (B6); the evaluation of the density terms in those equations giving a factor ρ_0 (see equation (A1), applied to the prolate spheroid). Then this central density ρ_0 will appear as an external factor in equation (B8), from which it can be obtained once we give M_{Bar}; thus the coefficients p_{0_n}, p_{1_n} are explicitly known, and so are the functions $\rho^\star_n(a)$. The set of functions $\rho^\star_n(a)$ is the function $\rho(a)$ needed in equations (B1) - (B4).

The integrals in equations (B1) - (B4) are evaluated with the intervals in a_n, and the corresponding values of β_p. For an external point $\mathbf{r} = (x, y, z)$ the values of β_p at the major semi-axes a_n are the solutions of

$$
x^2 \sin^2\beta_{p_n} + R^2 \tan^2\beta_{p_n} = a_n^2 e_p^2, \; n = 1, 2, ..., N_1 + N_2 + N_3 + 1.
\tag{B9}
$$

If the point $\mathbf{r}$ is inside the prolate spheroid, there is an $n_0 \in \{1, 2, ..., N_1 + N_2 + N_3\}$ such that $a_{n_0} \leq a(\mathbf{r}) \leq a_{n_0+1}$ ($a(\mathbf{r})$ is the major semi-axis of the *similar* spheroidal surface passing through the point $\mathbf{r}$). In this case the maximum β_{p_n} intervening in the integrals is $\beta_{p_{n_0}}$ given by $x^2 \sin^2\beta_{p_{n_0}} + R^2 \tan^2\beta_{p_{n_0}} = a_{n_0}^2 e_p^2$.

Thus, for an internal point $\mathbf{r}$ equations (B1) and (B2) are

$$
-\frac{\partial\Phi}{\partial x} = -4\pi\, e_p^{-3}\,(1 - e_p^2) x \left\{ \sum_{n=1}^{n_0-1} \int_{\beta_{p_n}}^{\beta_{p_{n+1}}} (p_{0_n} + \frac{p_{1_n}}{a_x} a(\beta_p)) \frac{\sin^2\beta_p}{\cos\beta_p} d\beta_p \right.
$$

$$+ \int_{\beta_{p n_0}}^{sin^{-1} e_p} (p_{0_{n_0}} + \frac{p_{1_{n_0}}}{a_x} a(\beta_p)) \frac{sin^2 \beta_p}{cos \beta_p} d\beta_p \Big\} , \tag{B10}$$

$$-\frac{\partial \Phi}{\partial R} = -4\pi e_p^{-3} (1 - e_p^2) R \Big\{ \sum_{n=1}^{n_0-1} \int_{\beta_{pn}}^{\beta_{p n+1}} \left(p_{0_n} + \frac{p_{1_n}}{a_x} a(\beta_p) \right) \frac{sin^2 \beta_p}{cos^3 \beta_p} d\beta_p$$

$$+ \int_{\beta_{p n_0}}^{sin^{-1} e_p} \left(p_{0_{n_0}} + \frac{p_{1_{n_0}}}{a_x} a(\beta_p) \right) \frac{sin^2 \beta_p}{cos^3 \beta_p} d\beta_p \Big\} , \tag{B11}$$

and the first terms in both equations are excluded if $n_0 = 1$. The integrals in equations (B10) and (B11) are analytically easy to find.

The potential at the internal point $\mathbf{r}$ (see equation (B3)) is

$$\Phi = -4\pi e_p^{-1} (1 - e_p^2) \Big\{ \sum_{n=1}^{n_0-1} \int_{a_n}^{a_{n+1}} \left(p_{0_n} + \frac{p_{1_n}}{a_x} a \right) a \ln \frac{1 + sin\beta_p}{cos\beta_p} da +$$

$$+ \int_{a_{n_0}}^{a(\mathbf{r})} \left(p_{0_{n_0}} + \frac{p_{1_{n_0}}}{a_x} a \right) a \ln \frac{1 + sin\beta_p}{cos\beta_p} da +$$

$$+ \frac{1}{2} \ln \frac{1 + e_p}{1 - e_p} \left[\int_{a(\mathbf{r})}^{a_{n_0+1}} \left(p_{0_{n_0}} + \frac{p_{1_{n_0}}}{a_x} a \right) a \, da + \sum_{n=n_0+1}^{N_1+N_2+N_3} \int_{a_n}^{a_{n+1}} \left(p_{0_{n_0}} + \frac{p_{1_{n_0}}}{a_x} a \right) a \, da \right] \Big\} , \tag{B12}$$

and we exclude the first or last sums if $n_0 = 1$ or $n_0 = N_1 + N_2 + N_3$, respectively.

With $I_n(a) = \int_0^a \rho_n^\star(u) u du = \frac{1}{2} p_{0_n} a^2 + \frac{1}{3} \frac{p_{1_n}}{a_x} a^3$, and integrating by parts, equation (B12) can be written as

$$\Phi = -4\pi e_p^{-1} (1 - e_p^2) \Big\{ - \sum_{n=1}^{n_0-1} \int_{\beta_{pn}}^{\beta_{p n+1}} I_n(a(\beta_p)) \frac{d\beta_p}{cos\beta_p} - \int_{\beta_{p n_0}}^{sin^{-1} e_p} I_{n_0}(a(\beta_p)) \frac{d\beta_p}{cos\beta_p} +$$

$$+ \sum_{n=1}^{n_0-1} \left[I_n(a_{n+1}) \ln \frac{1 + sin\beta_{p n+1}}{cos\beta_{p n+1}} - I_n(a_n) \ln \frac{1 + sin\beta_{pn}}{cos\beta_{pn}} \right] +$$

$$+\frac{1}{2}\ln\frac{1+e_p}{1-e_p}\left[I_{n_0}(a_{n_0+1})+\sum_{n=n_0+1}^{N_1+N_2+N_3}[I_n(a_{n+1})-I_n(a_n)]\right]-I_{n_0}(a_{n_0})\ln\frac{1+sin\beta_{p_{n_0}}}{cos\beta_{p_{n_0}}}\Bigg\},$$
$$(B13)$$

with the explicit form of $I_n(a)$, the integrals in this equation are also easy to solve analytically.

For an external point $\mathbf{r}$ the accelerations and potential are

$$-\frac{\partial\Phi}{\partial x}=-4\pi\,e_p^{-3}\,(1-e_p^2)x\sum_{n=1}^{N_1+N_2+N_3}\int_{\beta_{p_n}}^{\beta_{p_{n+1}}}(p_{0_n}+\frac{p_{1_n}}{a_x}a(\beta_p))\frac{sin^2\beta_p}{cos\beta_p}d\beta_p,\qquad(B14)$$

$$-\frac{\partial\Phi}{\partial R}=-4\pi e_p^{-3}(1-e_p^2)R\sum_{n=1}^{N_1+N_2+N_3}\int_{\beta_{p_n}}^{\beta_{p_{n+1}}}(p_{0_n}+\frac{p_{1_n}}{a_x}a(\beta_p))\frac{sin^2\beta_p}{cos^3\beta_p}d\beta_p,\qquad(B15)$$

$$\Phi=-4\pi e_p^{-1}(1-e_p^2)\left\{-\sum_{n=1}^{N_1+N_2+N_3}\int_{\beta_{p_n}}^{\beta_{p_{n+1}}}I_n(a(\beta_p))\frac{d\beta_p}{cos\beta_p}+\right.$$

$$+\sum_{n=1}^{N_1+N_2+N_3}\left[I_n(a_{n+1})\ln\frac{1+sin\beta_{p_{n+1}}}{cos\beta_{p_{n+1}}}-I_n(a_n)\ln\frac{1+sin\beta_{p_n}}{cos\beta_{p_n}}\right]\right\}.\qquad(B16)$$

C.   The Model of Superposition of Ellipsoids

One of the most conspicuous characteristics of the Galactic bar (also observed in other galaxies) is the "boxy" form of its isophotes (Freudenreich 1998; Zhao & Mao 1996; Ibata & Gilmore 1995). In the ellipsoidal and prolate models of the Galactic bar the iso-density contours are elliptical. In order to approximate the boxy iso-density contours we have considered a superposition of inhomogeneous ellipsoids.

The model consists of four ellipsoids with a density of the functional form given in equation (A1). The x, y, z-axes define the major, middle, and minor axes of the Galactic bar. Two identical ellipsoids have their major axes along the x-axis, and their middle and minor axes are rotated around the x-axis an angle θ_1 to both sides of the z-axis (see Figure

11 a). The other two ellipsoids, also identical, have their middle axes along the y-axis, and their major and minor axes are rotated around the y-axis an angle θ_2 to both sides of the z-axis (see Figure 11 b). The reason to try this arrangement of ellipsoids is simply that it favors the boxy edge-on appearance of the bar.

Our task is to find the dimensions, relative masses, and orientation angles θ_1, θ_2 of the four ellipsoids, such that their superposition gives a good approximation to MSF.

The ellipsoidal model in Section A has the effective semi-axes a_{Bar}, $b_{Bar} = a_{Bar}a_y$, $c_{Bar} = a_{Bar}a_z$, and corresponding scale lengths a_x, a_y, a_z. In its outer region the Gaussian factor has the scale length h_{end}. For the two identical ellipsoids rotated the angle θ_1 (see Fig. 11 a), we take their dimensions and scale lengths as $a_{Bar_1} = k_1 a_{Bar}$, $b_{Bar_1} = k_2 b_{Bar}$, $c_{Bar_1} = k_3 c_{Bar}$, $a_{x1} = k_1 a_x$, $a_{y1} = k_2 a_y$, $a_{z1} = k_3 a_z$, $h_{end1} = k_1 h_{end}$, and each ellipsoid with a mass M_1, which is a fraction k_4 of the total mass of the bar (= sum of masses of the four ellipsoids in the model): $M_1 = k_4 M_{Bar}$. Likewise, for the other two identical ellipsoids rotated the angle θ_2 (see Fig. 11 b), the dimensions, scale lengths, and masses are taken as $a_{Bar_2} = k_5 a_{Bar}$, $b_{Bar_2} = k_6 b_{Bar}$, $c_{Bar_2} = k_7 c_{Bar}$, $a_{x2} = k_5 a_x$, $a_{y2} = k_6 a_y$, $a_{z2} = k_7 a_z$, $h_{end2} = k_5 h_{end}$, $M_2 = k_8 M_{Bar}$. $k_1, k_2, ..., k_8$ are positive constants. The constraints are $2k_4 + 2k_8 = 1$ and $a_{Bar_1} > b_{Bar_1} > c_{Bar_1}$, $a_{Bar_2} > b_{Bar_2} > c_{Bar_2}$, i.e., $k_1/k_2 > a_y/a_x$, $k_2/k_3 > a_z/a_y$, $k_5/k_6 > a_y/a_x$, $k_6/k_7 > a_z/a_y$.

The density of each ellipsoid in the superposition has the form given in equation (A1), using the corresponding dimensions, scale lengths, and total mass of the ellipsoid. This density is computed in a Cartesian system whose axes are the principal axes of the ellipsoid. The required central density ρ_0 is obtained from an equation analogous to equation (A6), using a fine partition (N_1, N_2, N_3) (we take the same partition in the four ellipsoids of the model) and with the corresponding mass of the ellipsoid.

Thus, formally, with the dimensions, mass, and orientation of each ellipsoid, we can write the expression for the density due to the superposition, $\rho_{sup}(\mathbf{r})$, at any point $\mathbf{r} = (x, y, z)$ in the Cartesian system whose axes x, y, z are the principal axes of the bar (i.e., the x- and y- axes lie on the Galactic plane, and the z-axis is the rotation axis of the Galaxy).

Once the numbers $k_1, k_2, ..., k_8$ and θ_1, θ_2 are chosen, the surfaces $\rho_{sup}(\mathbf{r})/\rho_{sup}(0) = c = constant$ can be obtained, and thus compared with the corresponding surfaces $\rho_S(\mathbf{r})/\rho_S(0) = c = constant$ arising from MSF, whose density is of the type in equation (A1), but with R_S given by equation (2).

The procedure to obtain a fit to MSF by means of the proposed superposition of ellipsoids is as follows: due to the symmetry of the surfaces $\rho_{sup}(\mathbf{r})/\rho_{sup}(0) = c$ and

$\rho_S(\mathbf{r})/\rho_S(0) = c$, we only consider the octant $x \geq 0$, $y \geq 0$, $z \geq 0$. In this octant we take a fine mesh of radial directions given by spherical angles (φ, θ) (the z-axis being the polar axis). In the mesh points $(\varphi, \theta)_i$ we find the distances to the origin, r_{sup}, r_S, of the corresponding points on the surfaces $\rho_{sup}(\mathbf{r})/\rho_{sup}(0) = c$ and $\rho_S(\mathbf{r})/\rho_S(0) = c$. Thus, for n mesh points and m values of the constant c (i.e., comparing m pairs of surfaces), we minimize the quantity

$$D = \left\{ \frac{\sum_{j=1}^{m} \frac{c_j}{n} \sum_{i=1}^{n} (r_S - r_{sup})_{ij}^2}{\sum_{j=1}^{m} c_j} \right\}^{1/2}, \tag{C1}$$

which gives an rms separation in all the pairs of surfaces.

D is a function of the ten variables $k_l, k_2, ..., k_8, \theta_1, \theta_2$. We have employed the algorithm *amoeba* of Press *et al.* (1992) to minimize the function D in the 10-dimensional space $(k_1, k_2, ..., k_8, \theta_1, \theta_2)$, under the imposed constraints on the variables $k_1, k_2, ..., k_8$. The point $(k_1, k_2, ..., k_8, \theta_1, \theta_2)$ where the function D reaches its minimum value gives our best fit to MSF. We obtain the following values of the variables at this point

$$
\begin{aligned}
k_1 &= 1.1982 \\
k_2 &= 1.4086 \\
k_3 &= 0.8565 \\
k_4 &= 0.2600 \\
\theta_1 &= 0.6758 \text{ rad} \\
k_5 &= 1.1803 \\
k_6 &= 1.1941 \\
k_7 &= 1.0123 \\
k_8 &= 0.2400 \\
\theta_2 &= 0.2420 \text{ rad}
\end{aligned}
$$

With all these properties of the ellipsoids in the superposition, the potential and force field of each ellipsoid in its corresponding Cartesian axes are obtained with the procedure given in Section A for the ellipsoidal model. Thus, the potential and force field are obtained at any point $\mathbf{r} = (x, y, z)$ in the Cartesian system of the principal axes of the bar.

In figure 12 we show some iso-density contours on the three Cartesian planes, obtained with our superposition model (dark lines), and with MSF (light lines). Figure 13 shows the density of our model (continuous lines), and of MSF (dotted lines), along the three principal axes of the bar.

To see how MSF is approximated by the three proposed models of the Galactic bar, we can compare the weighted mean-squared separation $c_j < (\Delta r)^2 > \equiv \frac{c_j}{n} \sum_{i=1}^{n} (r_S - r_{mod})_{ij}^2$ between iso-density surfaces $\rho_S(\mathbf{r})/\rho_S(0) = c_j$, $\rho_{mod}(\mathbf{r})/\rho_{mod}(0) = c_j$, where mod indicates any of the three models. Figure 14 shows this comparison. Clearly, our third model gives a better approximation to MSF.

D. Analysis of Force Fields

In this section we give a brief analysis of the dependence of the force field obtained with the ellipsoidal, prolate, and superposition models (Sections A, B, and C of this Appendix) on the values of the partition numbers N_1, N_2, N_3. In the ideal limit these must be very large numbers, but it is important to find in each model a representative set (N_1, N_2, N_3) which shall give a gravitational field very similar to that obtained with large numbers, and not being excessively time-consuming in numerical orbital integrations.

Some tests showed that in the ellipsoidal and superposition models a partition with $N_1 + N_2 + N_3 \sim 100$ satisfy the time requirement, and gives a small rate of change of the force field under variations of N_1, N_2, N_3. For the prolate model, an appropriate partition has $N_1 + N_2 + N_3 \sim 30$; this reduction of components is expected since the linear functions employed in this model approximate the density function better, and a small number suffices.

To analyze in detail if the proposed values of $N_1 + N_2 + N_3$ are indeed appropriate, we have taken the definite numbers $N_1 = 20$, $N_2 = 65$, $N_3 = 15$ in the ellipsoidal and superposition models, and $N_1 = 15$, $N_2 = 20$, $N_3 = 5$ in the prolate model, with $a_L = 1$ kpc (see Section A) in all cases. Also, we take the mass of the bar as 9.8×10^9 M$\odot$ (see Section 2).

Keeping a_L fixed, we increase the partition numbers by a certain factor and compute the resulting force (acceleration) F along the principal axes of the bar. This force is compared at corresponding distances on a given axis with the force F_0 obtained using the numbers given above, and we find the maximum relative difference $|\Delta F/F| = |(F - F_0)/F|$ from the three axes. Figure 15 shows the results of this analysis. The conclusion from this figure is that the partitions $(N_1, N_2, N_3)_0 = (20, 65, 15)$ in the ellipsoidal and superposition models, and $(N_1, N_2, N_3)_0 = (15, 20, 5)$ in the prolate model, give a force field, $\mathbf{F_0}$, which differs $\sim 2.5\%$ and 0.6%, respectively, from that obtained in the ideal limit of very large partition numbers. Finally, Figure 16 shows the acceleration along the three principal axes obtained with the partitions $(N_1, N_2, N_3)_0$. The superposition model differs significantly

from the ellipsoidal and prolate models.

REFERENCES

Alard, C. 2001, A&A, 379, 44

Allen, C. 1990, RMxAA, 20, 67

Allen, C., & Martos, M. A. 1988, RMxAA, 16, 25

Allen, C., & Santillán, A. 1991, RMxAA, 22, 255

Athanassoula, E., 1990, in Annals New York Academy of Sciences, V. 596, p. 181. Editors: J. R. Buchler, S. T. Gottesman, & J. H. Hunter Jr.

Athanassoula, E., Bienaymé, O., Martinet, L., & Pfenniger, D. 1983, 127, 349

Beaulieu, S. F., Freeman, K. C., Kalnajs, A. J., Saha, P, Zhao, H. 2000, AJ, 120, 855

Binney, J., Gerhard, O. E., Stark, A. A., Bally, J., & Uchida, K. I. 1991, MNRAS, 252, 210

Binney, J., Gerhard, O. E., & Spergel, D. N. 1997, MNRAS, 288, 365

Bissantz, N., Englmaier, P., & Gerhard, O. 2003, MNRAS, 340, 949

Bissantz, N., & Gerhard, O. 2002, MNRAS, 330, 591

Brosche, P., Odenkirchen, M., & Geffert, M. 1999, New Astronomy, 4, 133

Brosche, P., Tucholke, H.-J., Klemola, A. R., Ninkovic, S., Geffert, M., & Doerenkamp, P. 1991, AJ, 102, 2022

Combes, F., & Elmegreen, B. G. 1993, A&A, 271, 391

Contopoulos, G., & Papayannopoulos, T. 1980, A & A, 93, 33

Dauphole, B., Geffert, M., Colin, J., Ducourant, C., Odenkirchen, M., & Tucholke, H.-J. 1996, A & A, 313, 119

Debattista, V. P., Gerhard, O., & Sevenster, M. N. 2002, MNRAS, 334, 355

Dehnen, W. 2000, AJ, 119, 800

Dinescu, D. I., Girard, T. M., & van Altena, W. F. 1999, AJ, 117, 1792

Dwek, E., Arendt, R. G., Hauser, M. G., Kelsall, T., Lisse, C. M., Moseley, S. H., Silverberg, R. F., Sodroski, T. J., & Weiland, J. L. 1995, 445, 716

Englmaier, P., & Gerhard, O. 1999, MNRAS, 304, 512

Ferrers, N. M., 1877, *Quart. J. Pure Appl. Math.*, 14, 1

Freudenreich, H. T. 1998, ApJ, 492, 495

Fux, R. 1997, A&A, 327, 983

Fux, R. 1999, A&A, 345, 787

Fux, R., 2001, A&A, 373, 511

Gerhard, O. E., & Vietri, M. 1986, MNRAS, 223, 377

Gerhard, O. E. 2002, ASP, 273, 73

Harmon, R., & Gilmore, G. 1988, MNRAS, 235, 1025

Hasan H., & Norman, C., 1990, ApJ, 361, 69

Hernquist, L., & Ostriker, J. P. 1992, ApJ, 386, 375

Ibata, R. A., & Gilmore, G. F. 1995, MNRAS, 275, 605

Kaufmann, D. E., & Contopoulos, G. 1996, 309, 381

Kellogg, O. D. 1953, *Foundations of Potential Theory.* New York: Dover

Kent, S.M., 1992, ApJ, 387, 181

Lerner, M. S., Sundin, M., & Thomasson, M. 1999, A&A, 344, 483

Liszt, H. S., & Burton, W. B. 1980, ApJ, 236, 779

Matsumoto, T., Hayakawa, S., Koizumi, H., Murakami, H., Uyama, K., Yamagami, T., & Thomas, J.A., 1982, Proceedings of the Workshop *IN: The galactic center*, Pasadena, CA, p.48

Mc. Millan, W. D. 1930, The Theory of the Potential (Dover Publications: New York)

Nakada, Y., Deguchi, S., Hashimoto, O., Hizumiura, H., Onaka, T., Sekiguchi, K., & Yamamura, I. 1991, Nature, 353, 140

Nikolaev, S., & Weinberg, M. D. 1997, ApJ, 487, 885

Norman, C. A., Sellwood, J. A., & Hasan, H. 1996, ApJ, 462, 114

Papayannopoulos, T., & Petrou, M. 1983, A & A, 119, 21

Petrou, M., & Papayannopoulos, T. 1983, MNRAS, 219, 157

Pfenniger, D. 1984, A& A, 134, 373

Pichardo, B., Martos, M., Moreno, E., & Espresate, J. 2003, ApJ, 582, 230

Press, W. H., Teukolsky, S. A., Vetterling, W. T., & Flannery, B. P. 1992, Numerical
    Recipes in Fortran 77: The Art of Scientific Computing, 2nd. ed. (Cambridge
    University Press: Cambridge)

Pryor, C., & Meylan, G. 1993, in ASP Conf. Ser. 50, Structure and Dynamics of Globular
    Clusters, ed. S. G. Djorgovski & G. Meylan (San Francisco: ASP), 357

Sanders, R. H., & Prendergast, K. H. 1974, ApJ, 188, 489

Sanders, R. H., & Tubbs, A. D. 1980, ApJ, 235, 803

Sevenster, M. N. 1999, MNRAS, 310, 629

Schmidt, M. 1956, B. A. N. 13, 15

Shlosman, I., & Heller, C. H. 2002, ApJ, 565, 921

Teuben, P. J., & Sanders, R. H. 1985, MNRAS, 212, 257

Tremaine, S., & Weinberg, M. D. 1984, ApJ, 282, 5

Weiland, J. L., Arendt, R. G., Berriman, G. B., Dwek, E., Freudenreich, H. T., Hauser, M.
    G., Kelsall, T., Lisse, C. M., Mitra, M., & Moseley, S. H. 1994, ApJ, 425, 81

Weiner, B. J., & Sellwood, J. A. 1999, ApJ, 524, 112

Weinberg, M. D. 1992, ApJ, 384, 81

Zhao, H. 1996, MNRAS, 278, 488

Zhao, H. 2000, MNRAS, 316, 418

Zhao, H., & Mao, S. 1996, MNRAS, 283, 1197

TABLE 1

Orbital Properties in the Axisymmetric Galactic Model

of Allen & Santillán (1991)

NGC	$< r_{min} >$	$< r_{max} >$	$< |z|_{max} >$	$< e >$	E	h
5139	1.11	6.97	0.69	0.72	-1492.5	-42.4
6093	0.58	3.67	1.52	0.73	-1713.5	-6.0
6144	2.22	2.82	2.48	0.12	-1663.9	-20.3
6171	2.82	3.79	2.23	0.15	-1578.2	46.9
6218	3.02	5.74	2.44	0.31	-1458.9	64.3
6712	1.14	6.75	1.93	0.71	-1478.7	22.3

Distances in kpc; E in units of 100 km^2 s^{-2}; h in units of 10 km s^{-1} kpc.

TABLE 2
Orbital Properties with the three Models of the Galactic Bar

NGC	$< r_{min} >$	$< r_{max} >$	$< |z|_{max} >$	$< e >$	E_{min}	E_{max}	h_{min}	h_{max}
5139	1.62	6.37	1.71	0.58	-1554.6	-1375.3	-52.7	-22.8
	1.01	8.14	1.41	0.77	-1561.9	-1314.6	-53.9	-12.7
	1.15	8.39	2.42	0.76	-1538.4	-1304.3	-50.0	-11.0
6093	0.69	4.00	1.50	0.69	-1851.9	-1523.7	-30.4	24.3
	0.81	4.00	1.61	0.65	-1769.8	-1550.3	-16.6	20.0
	1.55	2.90	2.52	0.31	-1753.7	-1664.8	-14.4	0.4
6144	2.30	3.23	2.90	0.17	-1675.0	-1567.5	-23.8	-5.9
	1.83	3.45	2.57	0.31	-1715.0	-1551.4	-30.4	-3.1
	1.98	3.46	2.78	0.28	-1684.5	-1563.1	-25.9	-5.7
6171	1.57	3.65	1.49	0.42	-1843.1	-1482.9	3.3	63.4
	2.00	3.58	1.83	0.30	-1838.3	-1451.4	4.2	68.7
	2.03	3.24	1.95	0.22	-1793.6	-1455.2	11.7	68.1
6218	2.16	4.51	2.01	0.36	-1783.9	-1415.2	10.7	72.2
	2.94	5.93	2.35	0.34	-1521.4	-1378.8	54.5	78.3
	2.23	5.11	1.89	0.40	-1750.1	-1406.4	16.6	73.9
6712	1.03	6.14	2.39	0.70	-1595.8	-1353.9	4.1	44.4
	1.00	6.72	1.72	0.75	-1603.4	-1401.5	2.8	36.5
	0.98	6.60	1.77	0.74	-1601.5	-1418.7	3.5	34.0

-Distances in kpc; E in units of 100 km^2 s^{-2}; h in units of 10 km s^{-1} kpc.

-Lines in each entry: first: ellipsoidal model, second: prolate model,

third: superposition model.
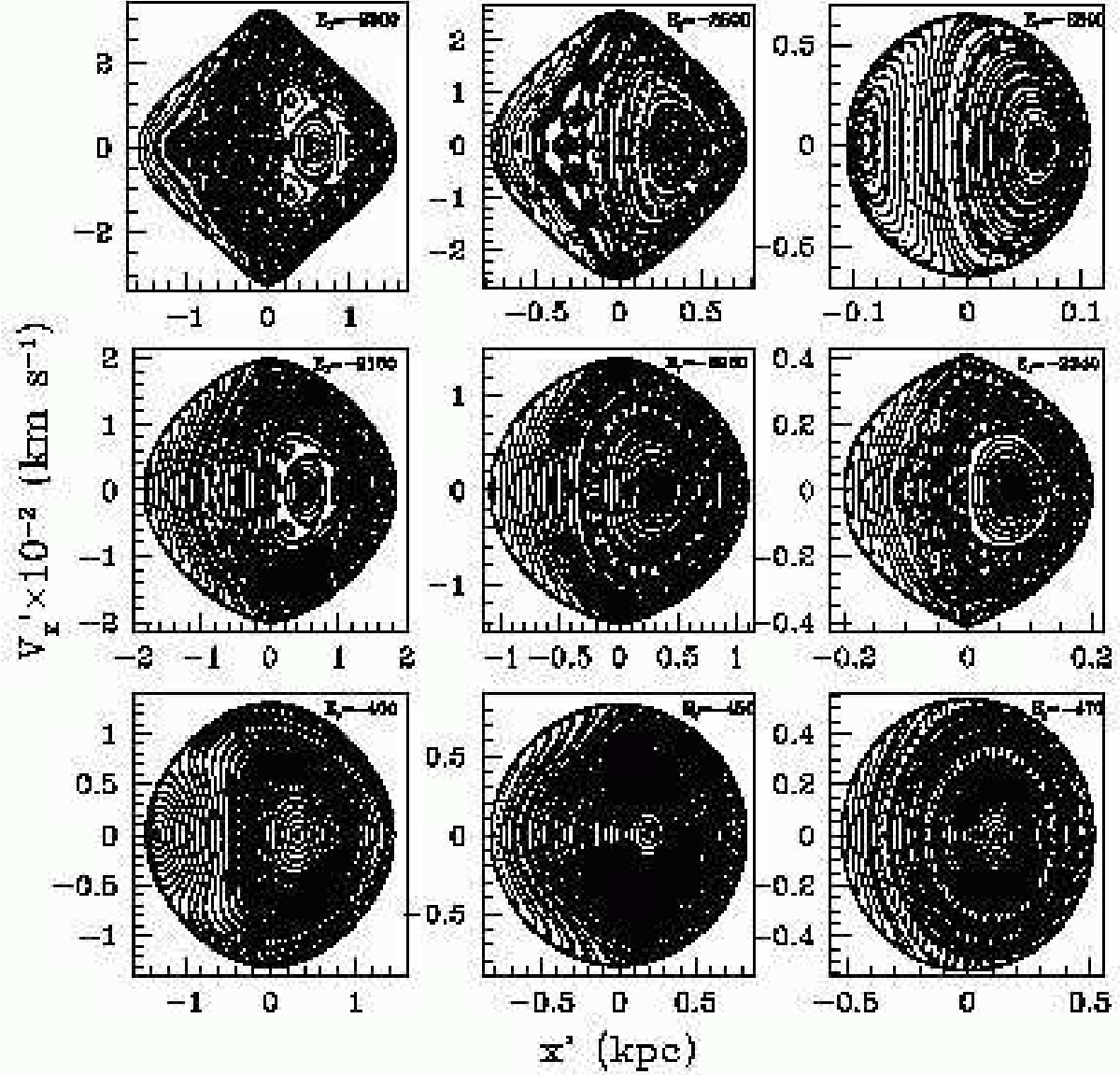
Fig. 1.— Three examples of Poincaré diagrams using the ellipsoidal model, for experiments I, II and III, from top to bottom. In all cases the darkest regions represent the orbits in the *separatrix*. The units of Jacobi's constant, E_J, are 100 km^2 s^{-2}
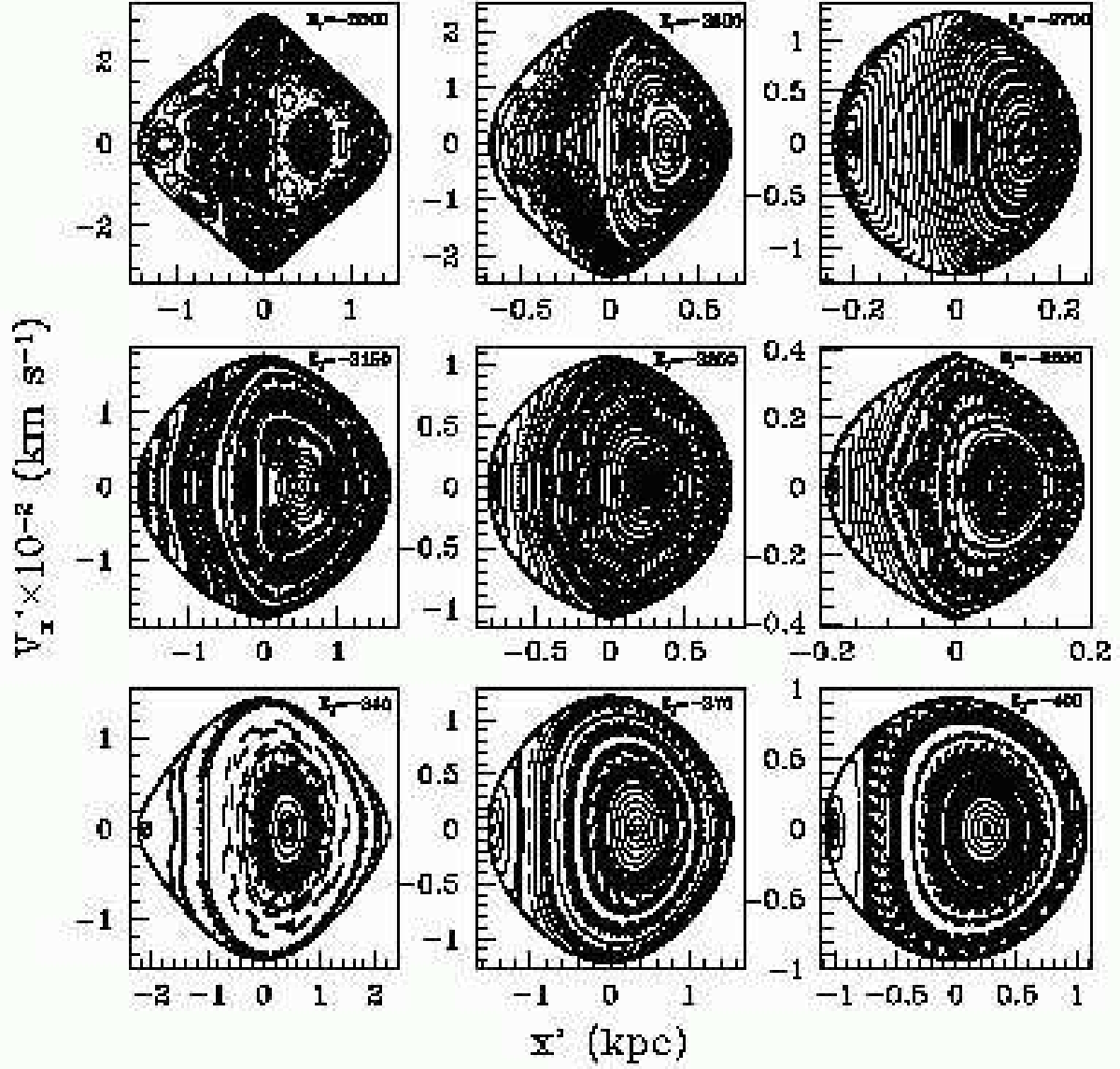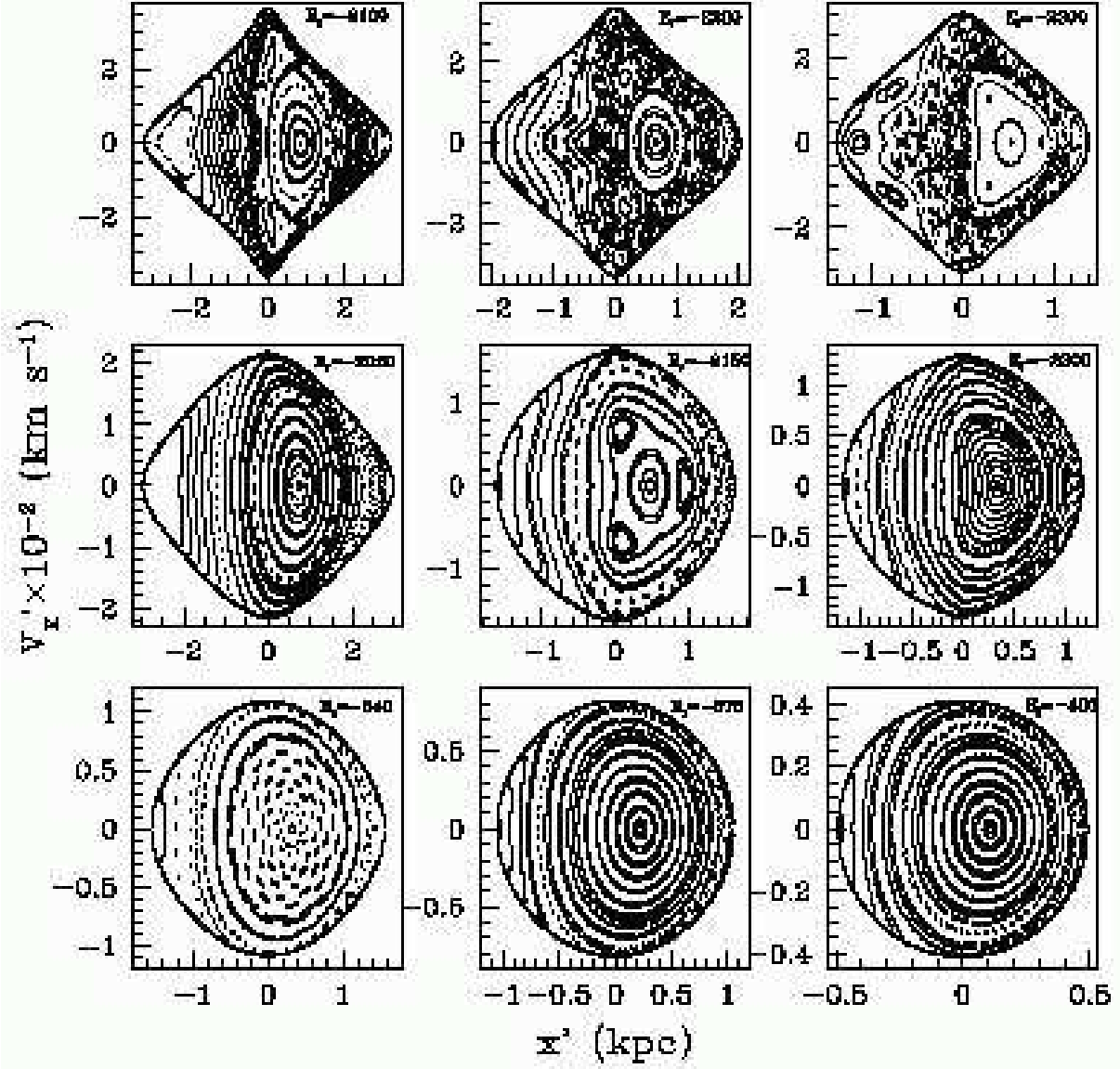
Fig. 2.— Same as in Figure 1, using the prolate model.

– 31 –

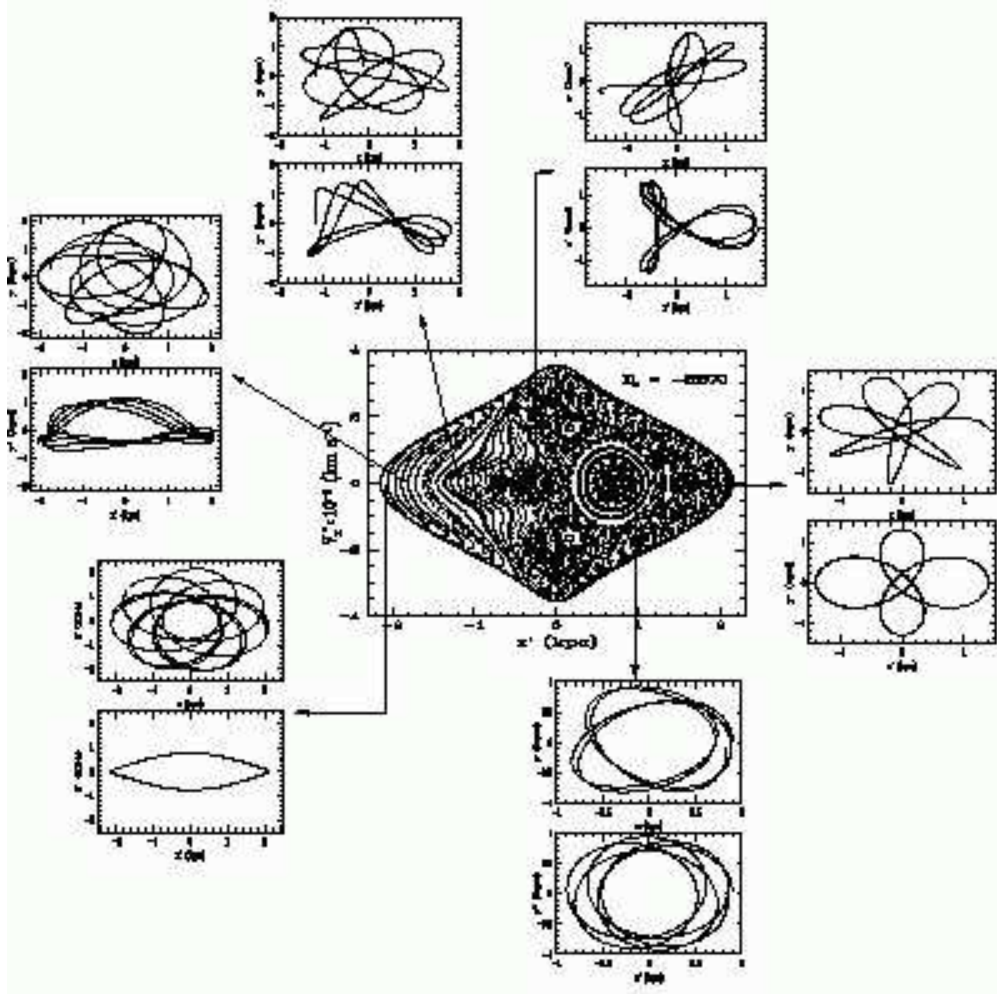Fig. 3.— Same as in Figure 1, using the superposition model.

Fig. 4.— Some examples of orbits in configuration space with the ellipsoidal model for experiment I; the orbits are extracted from a given orbital family. Top panels of each frame correspond to the inertial reference frame, and bottom panels to the non-inertial frame that rotates with the bar.
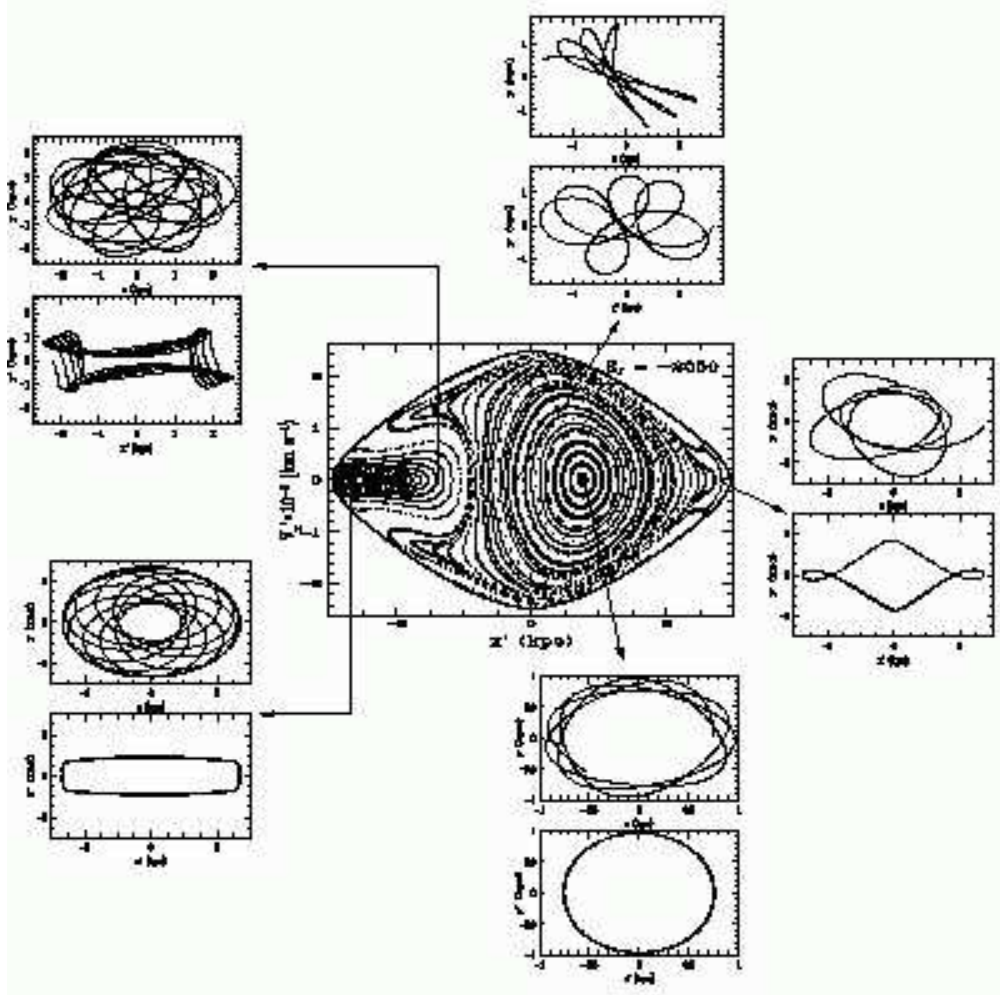
Fig. 5.— Same as in Figure 4, for experiment II.
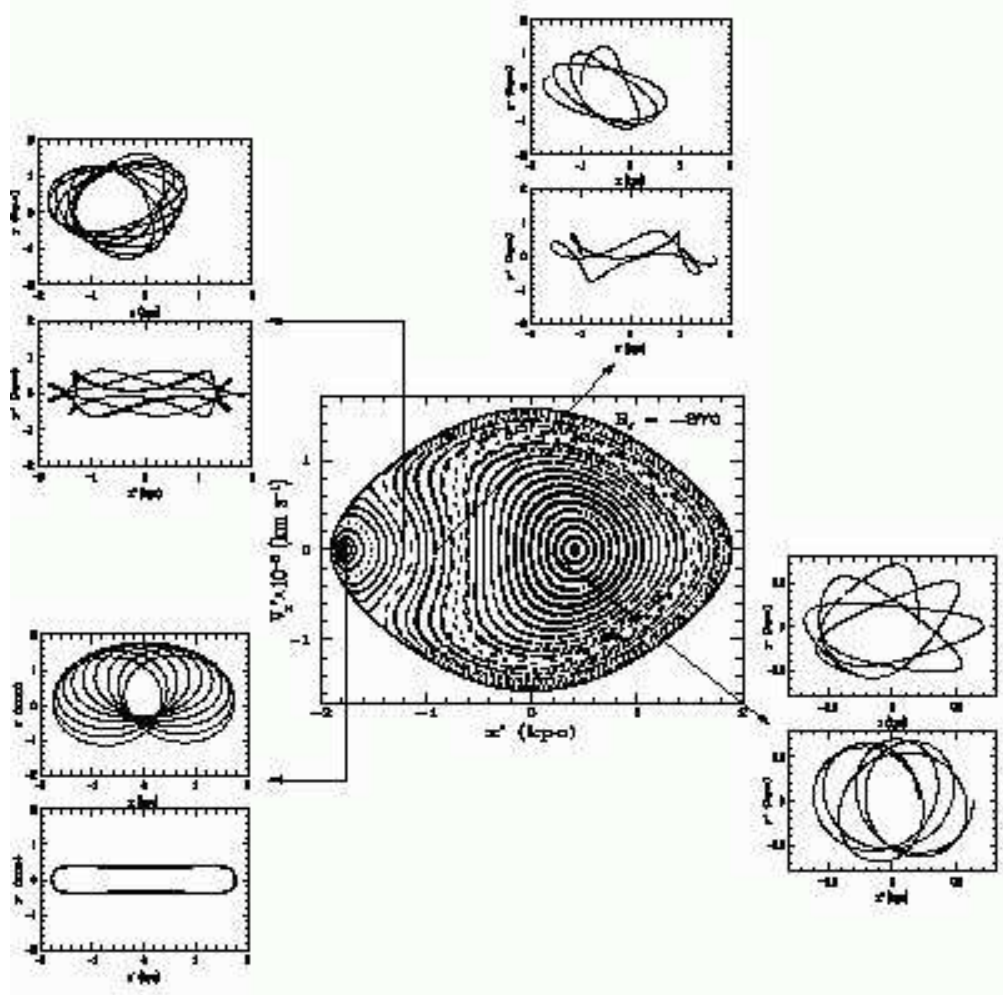
Fig. 6.— Same as in Figure 4, for experiment III.
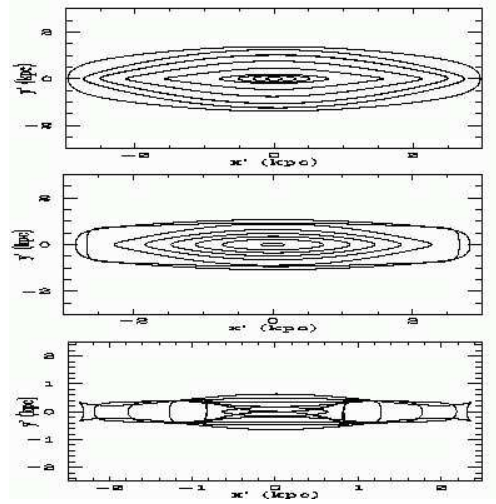
Fig. 7.— Some examples of x_1 periodic orbits with the ellipsoidal model for experiments I (top panel), II (middle panel), III (bottom panel)
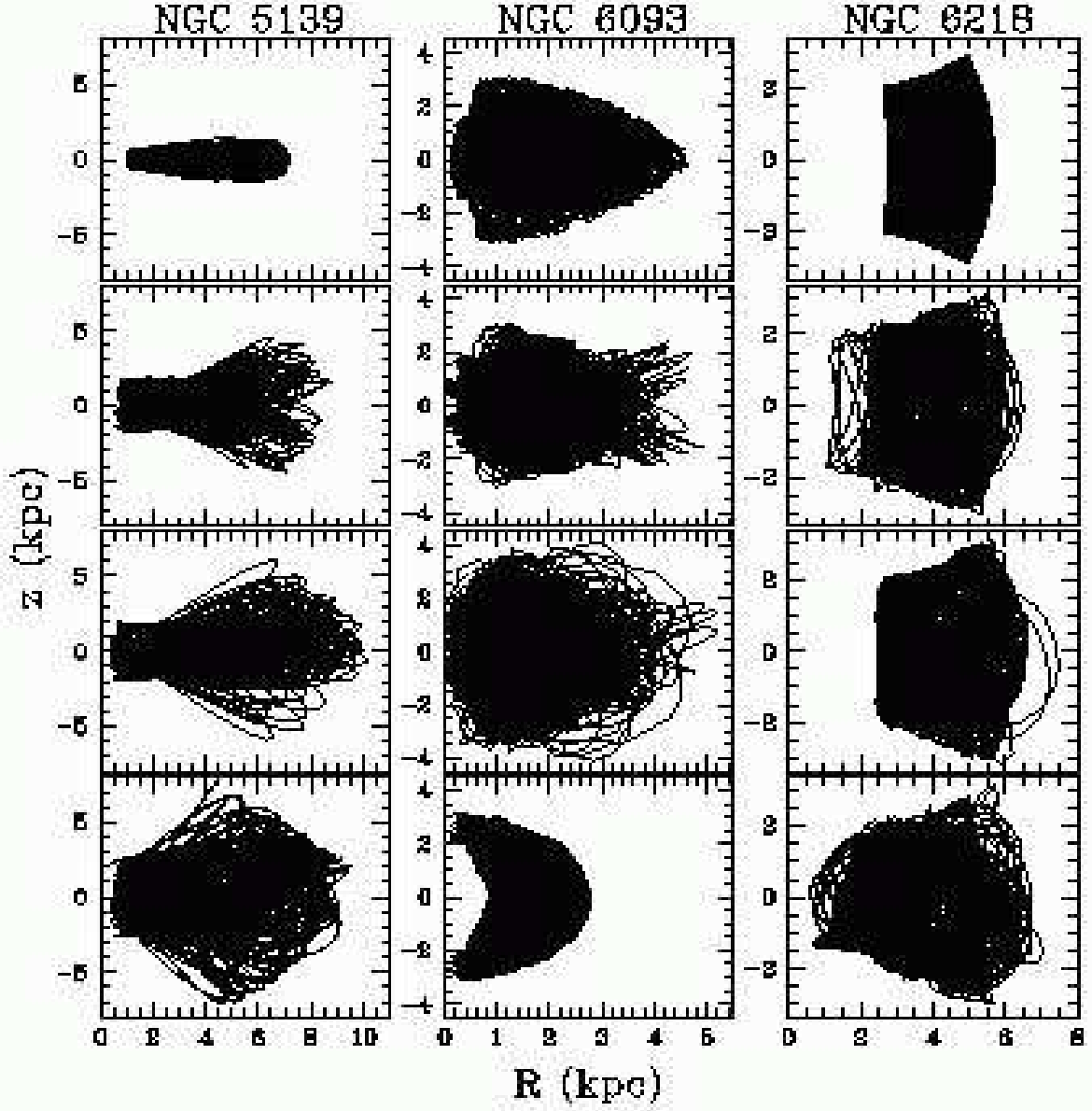
Fig. 8.— Meridional orbits of NGC 5139 (left column), NGC 6093 (middle column), and NGC 6218 (right column). The orbits in the upper panels are computed with the axisymmetric Galactic model of Allen & Santillán (1991). The second, third, and fourth rows give the orbits in a Galactic model using the ellipsoidal, prolate, and superposition models of the Galactic bar, respectively.
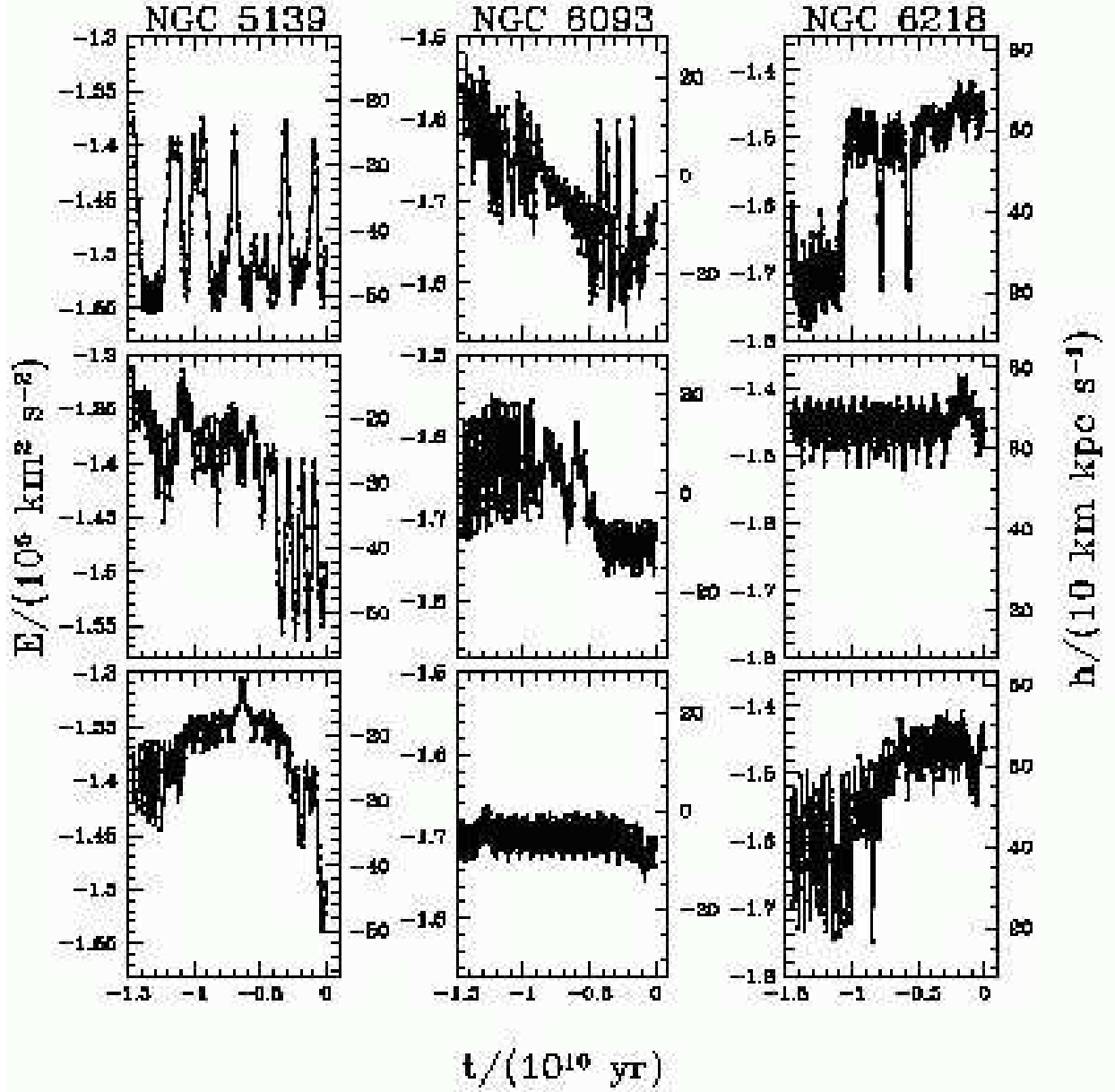
Fig. 9.— Variations of E and h in the orbits of NGC 5139, NGC 6093, and NGC 6218. Upper panels: ellipsoidal model of the bar; middle panels: prolate model; bottom panels: superposition model. E is read on the left scale, h on the right scale.
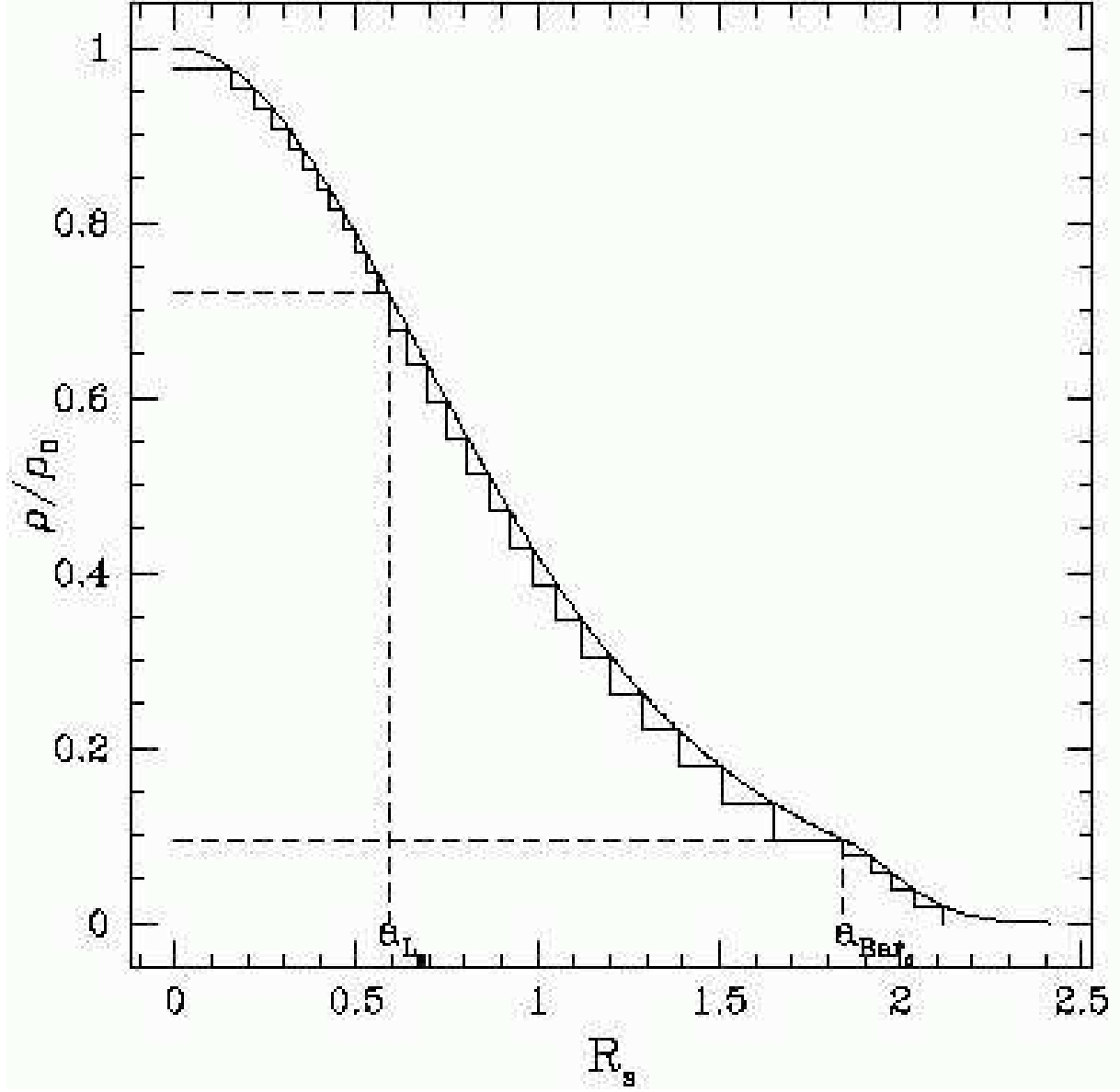
Fig. 10.— Superposition of homogeneous ellipsoidal components to approximate the density law of the Galactic bar. In the vertical axis the three intervals in density are shown. In this example, $a_L = 1$ kpc, $N_1 = 12$, $N_2 = 15$, $N_3 = 5$. a_{L_S} and a_{Bar_S} are the scaled a_L and a_{Bar} -i.e. divided by the scale length-.
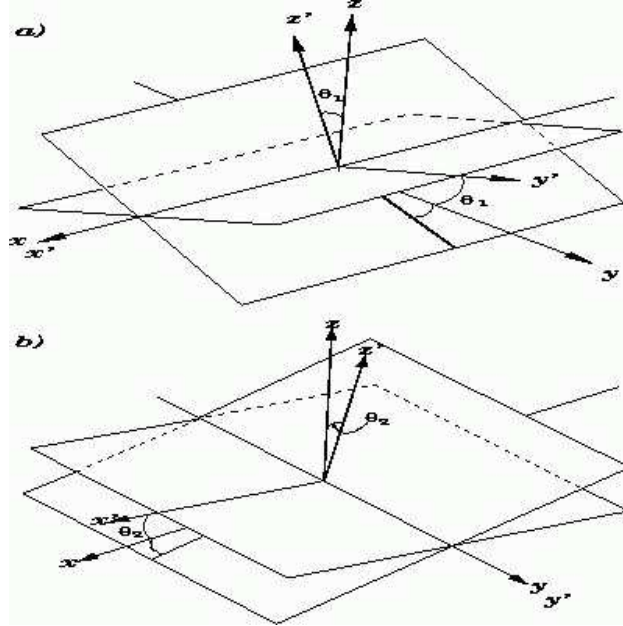
Fig. 11.— The planes that contain the major and middle axes of the four ellipsoids in our third model. In (a) two identical ellipsoids have their major axes, x', along the x-axis and their middle, y', and minor, z', axes rotated an angle θ_1 around the x-axis, to both sides of the z-axis. In (b) we show the orientation of the other two ellipsoids, with their middle axes, y', along the y-axis and their major, x', and minor, z', axes rotated an angle θ_2 around the y-axis, to both sides of the z-axis. Our model is the superposition of the ellipsoids in (a) and (b).
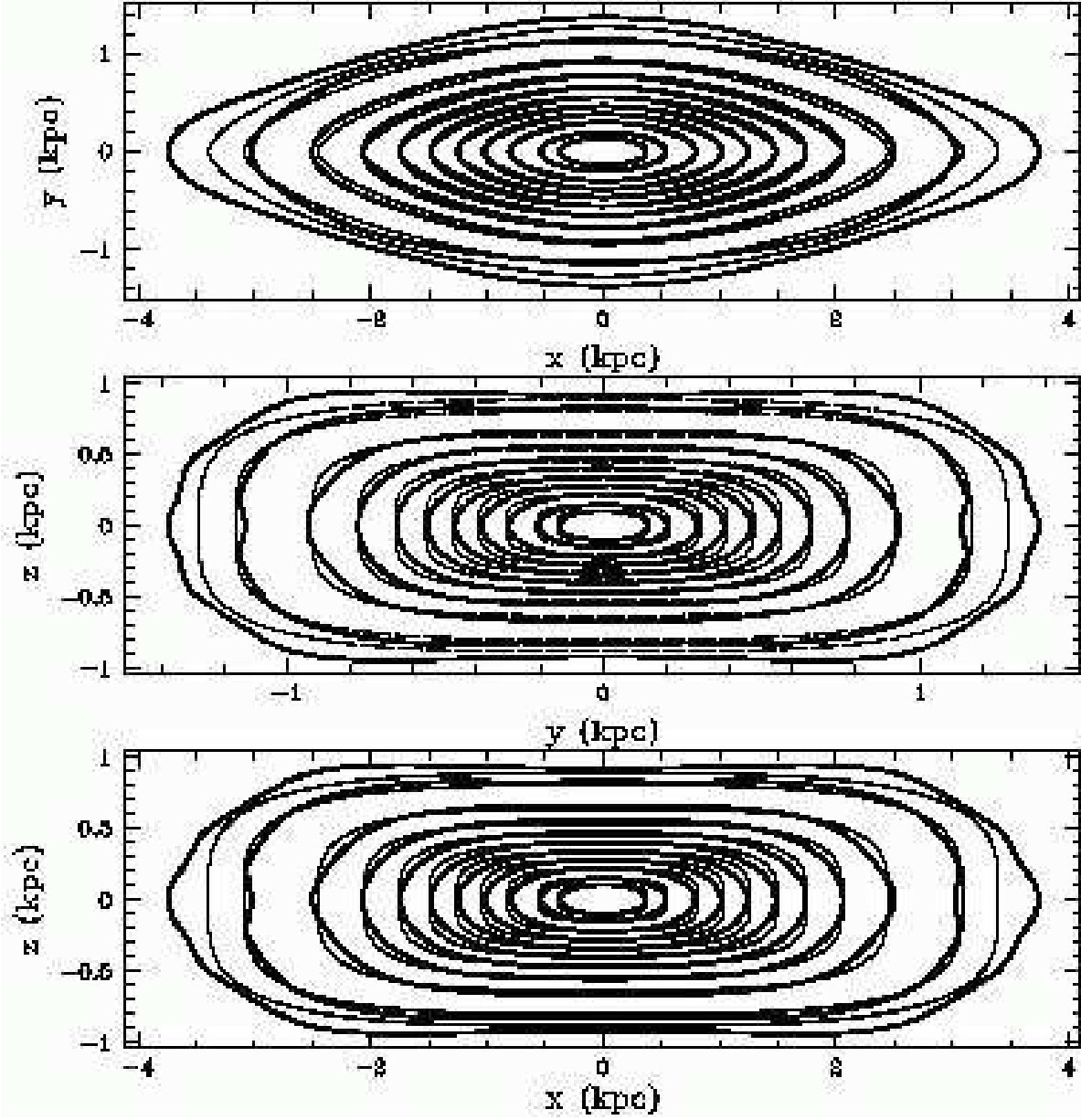
Fig. 12.— Iso-density contours on the $x - y$ plane -the Galactic plane- (top panel), $y - z$ plane (middle panel), and $x - z$ plane (bottom panel) of our third model for the Galactic bar (dark lines), and of Model S of Freudenreich (1998) (MSF) (light lines). The comparison is made for values of the constant c (see text) = 0.95, 0.9, 0.8, 0.7, 0.6, 0.5, 0.4, 0.3, 0.2, 0.1, and 0.05 . It is worth noticing that the scale in the three figures is not the same.
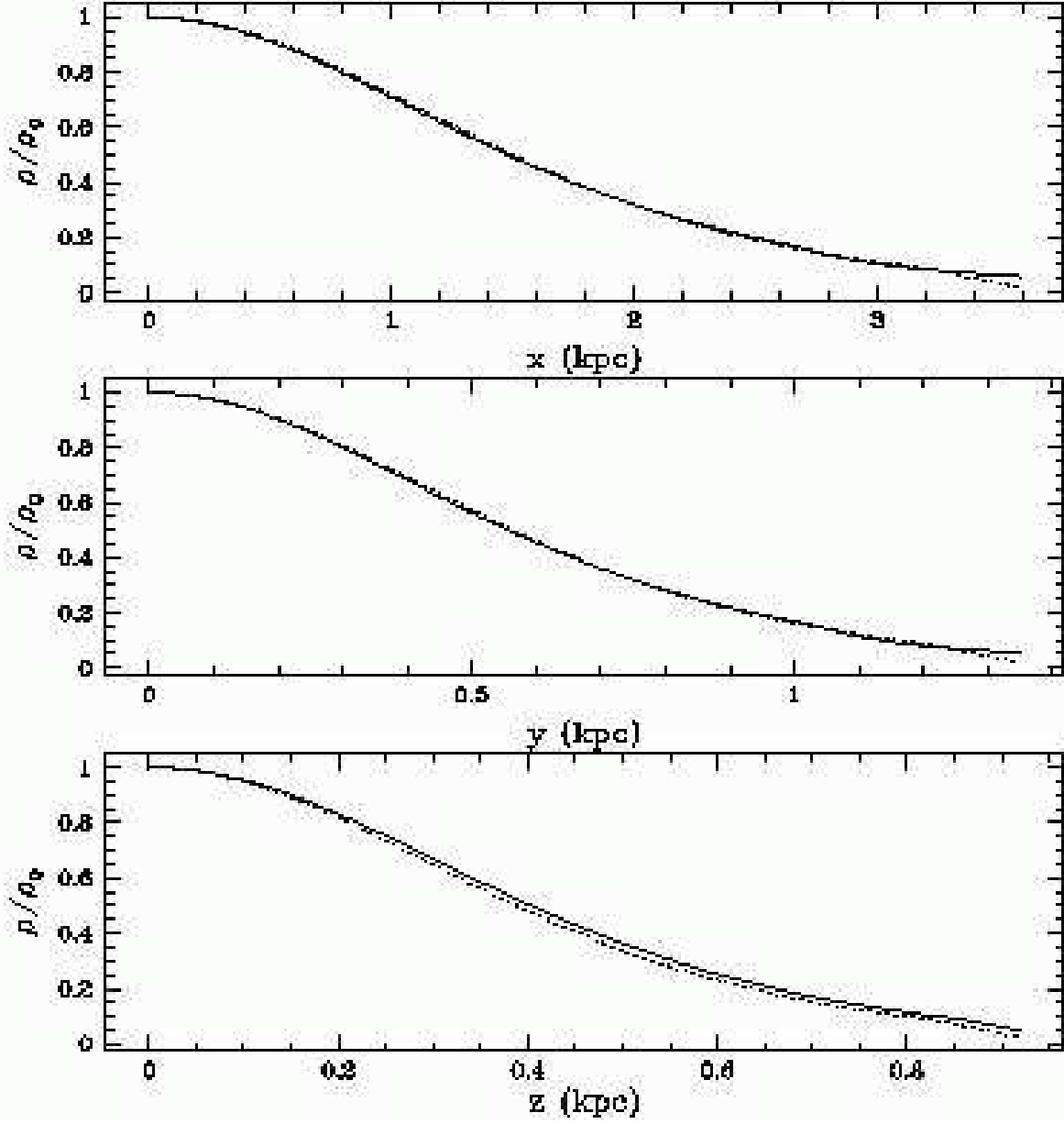
Fig. 13.— Density along the x-axis (top panel), y-axis (middle panel), and z-axis (bottom panel) -which represent the major, middle, and minor axes, respectively, of the bar- in our third model for the Galactic bar (continuous line), and for Model S of Freudenreich (1998) (MSF) (dotted lines).
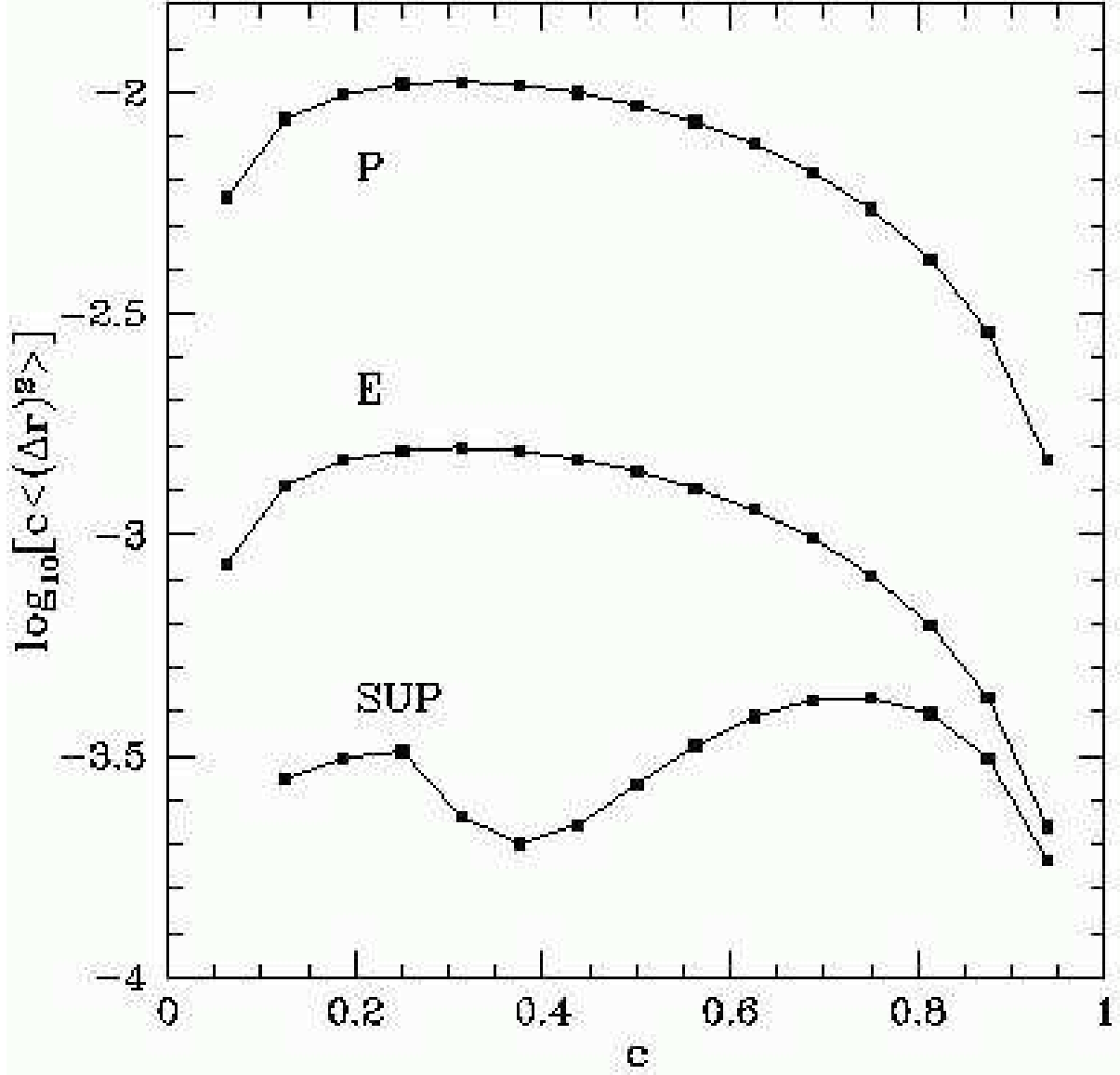
Fig. 14.— The weighted mean-squared separation between iso-density surfaces, $\rho/\rho_0 = c$, in Model S of Freudenreich (1998, MSF) and corresponding surfaces in our three models (E: ellipsoidal, P: prolate, SUP: superposition of ellipsoids).
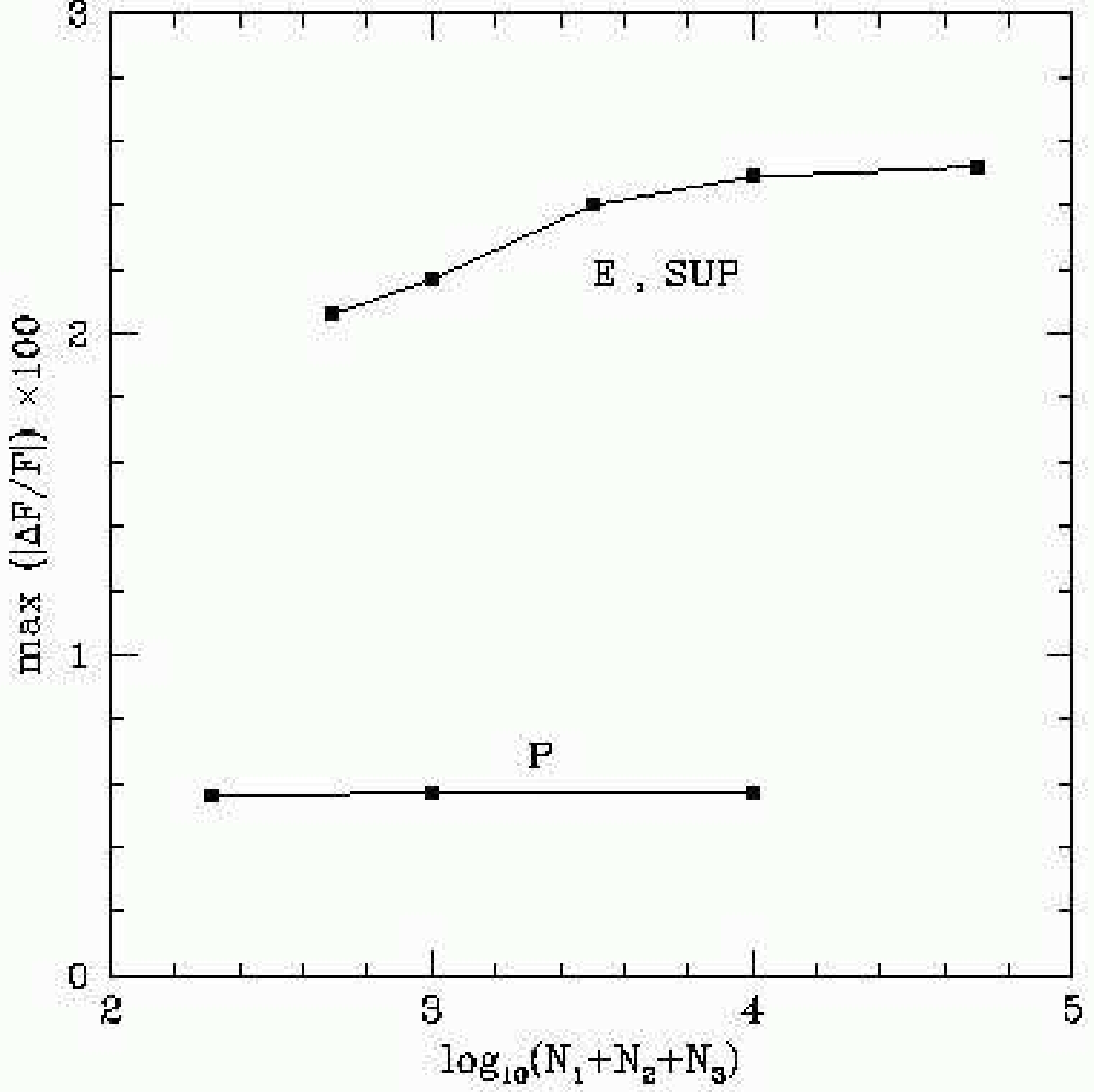
Fig. 15.— Percentage force difference comparing the force obtained with the partition numbers $(N_1, N_2, N_3)_0 = (20, 65, 15)$ in the ellipsoidal (E) and superposition (SUP) models, $(N_1, N_2, N_3)_0 = (15, 20, 5)$ in the prolate (P) model, and the force obtained with increasing partition numbers.
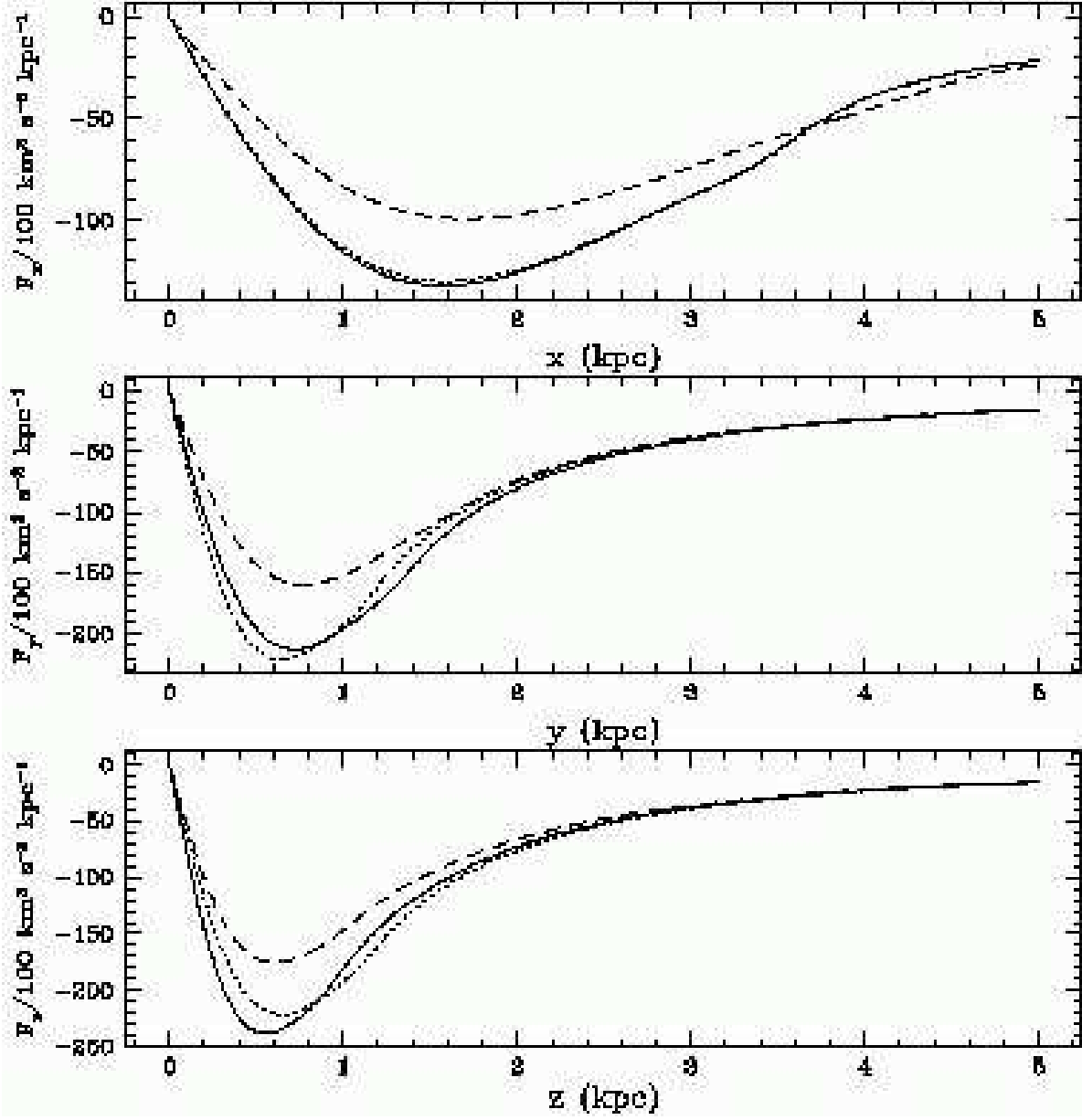
Fig. 16.— Acceleration along the x-axis (top panel), y-axis (middle panel), and z-axis (bottom panel), with the partition $(N_1, N_2, N_3)_0 = (20, 65, 15)$ in the ellipsoidal (continuous line) and superposition (discontinuous line) models, and with $(N_1, N_2, N_3)_0 = (15, 20, 5)$ in the prolate model (dotted line).